SANDIA REPORT

SAND87—1650 • UC—28
Unlimited Release
Printed September 1987

RS-8232-2/ 66239
C1

Predicted Radiation Environment of the Saturn Baseline Diode

8232-2//066239
00000001 -

J. A. Halbleib, J. R. Lee

Prepared by
Sandia National Laboratories
Albuquerque, New Mexico 87185 and Livermore, California 94550
for the United States Department of Energy
under Contract DE-AC04-76DP00789

SF2900Q(8-81)

1102012

Issued by Sandia National Laboratories, operated for the United States Department of Energy by Sandia Corporation.

NOTICE: This report was prepared as an account of work sponsored by an agency of the United States Government. Neither the United States Government nor any agency thereof, nor any of their employees, nor any of their contractors, subcontractors, or their employees, makes any warranty, express or implied, or assumes any legal liability or responsibility for the accuracy, completeness, or usefulness of any information, apparatus, product, or process disclosed, or represents that its use would not infringe privately owned rights. Reference herein to any specific commercial product, process, or service by trade name, trademark, manufacturer, or otherwise, does not necessarily constitute or imply its endorsement, recommendation, or favoring by the United States Government, any agency thereof or any of their contractors or subcontractors. The views and opinions expressed herein do not necessarily state or reflect those of the United States Government, any agency thereof or any of their contractors or subcontractors.

Printed in the United States of America
Available from
National Technical Information Service
U.S. Department of Commerce
5285 Port Royal Road
Springfield, VA 22161

NTIS price codes
Printed copy: A05

Category UC-28

SAND87-1650

Unlimited Release

Printed September 1987

Predicted Radiation Environment of the Saturn Baseline Diode

J. A. Halbleib and J. R. Lee
Simulation Physics Division
Sandia National Laboratories, P. O. Box 5800, Albuquerque, NM 87185

Abstract

Coupled electron/photon Monte Carlo radiation transport was used to predict the radiation environment of the Saturn accelerator for the baseline diode design. The X-ray output has been calculated, as well as energy deposition in CaF_2 thermoluminescent dosimetry and silicon. It is found that the design criteria for the radiation environment will be met and that approximately 10 kJ of X rays will be available for simulation experiments, if the diode provides a nominal beam of 2.0-MeV electrons for 20 ns with a peak current of 12.5 MA. The penalty in dose and X-ray output for operating below the nominal energy in order to obtain a softer spectrum is quantified. The penalty for using excessive electron equilibration in the standard packaging of the thermoluminescent dosimeters is shown to be negligible. An intrinsic lack of electron equilibration for silicon elements of components and subsystems is verified for Saturn environments, demonstrating the ambiguity of design criteria based on silicon deposition. Validation of an efficient next-event-estimator method for predicting energy deposition in equilibrated detectors/dosimetry is confirmed. Finally, direct-electron depositions in excess of 1 kJ/g are shown to be easily achievable.

Acknowledgements

We would like to thank Michele Song for preparing this manuscript. This work was supported by the U.S. Department of Energy under contract DE-AC04-76DP00789.

Table of Contents

Page

1. Introduction 11

2. Description of the Saturn Baseline Diode 13

3. Description of the Calculational Model 16

4. X-Ray Output 18

4.1 X-Ray Extraction Efficiency 19

4.2 Differential X-Ray Distributions 26

5. X-Ray Energy Deposition 33

5.1 TLD Dosimetry 35

5.1.1 The NE Method 35

5.1.2 The FT Method 44

5.2 Si Dose 48

5.2.1 Relative to TLD Dose 49

5.2.2 Free-Field Energy Deposition 55

6. Primary Electron Deposition in the Converter Configuration .. 61

7. Conclusions 63

References 67

Appendix 73

Distribution 82

Table of Contents

Page

1. Introduction 11

2. Description of the Saturn Baseline Diode 13

3. Description of the Calculational Model 16

4. X-Ray Output 18

4.1 X-Ray Extraction Efficiency 19

4.2 Differential X-Ray Distributions 26

5. X-Ray Energy Deposition 33

5.1 TLD Dosimetry 35

5.1.1 The NE Method 35

5.1.2 The FT Method 44

5.2 Si Dose 48

5.2.1 Relative to TLD Dose 49

5.2.2 Free-Field Energy Deposition 55

6. Primary Electron Deposition in the Converter Configuration .. 61

7. Conclusions 63

References 67

Appendix 73

Distribution 82

Table of Contents

Page

1. Introduction 11

2. Description of the Saturn Baseline Diode 13

3. Description of the Calculational Model 16

4. X-Ray Output 18

4.1 X-Ray Extraction Efficiency 19

4.2 Differential X-Ray Distributions 26

5. X-Ray Energy Deposition 33

5.1 TLD Dosimetry 35

5.1.1 The NE Method 35

5.1.2 The FT Method 44

5.2 Si Dose 48

5.2.1 Relative to TLD Dose 49

5.2.2 Free-Field Energy Deposition 55

6. Primary Electron Deposition in the Converter Configuration .. 61

7. Conclusions 63

References 67

Appendix 73

Distribution 82

Table of Contents

Page

1. Introduction 11

2. Description of the Saturn Baseline Diode 13

3. Description of the Calculational Model 16

4. X-Ray Output 18

4.1 X-Ray Extraction Efficiency 19

4.2 Differential X-Ray Distributions 26

5. X-Ray Energy Deposition 33

5.1 TLD Dosimetry 35

5.1.1 The NE Method 35

5.1.2 The FT Method 44

5.2 Si Dose 48

5.2.1 Relative to TLD Dose 49

5.2.2 Free-Field Energy Deposition 55

6. Primary Electron Deposition in the Converter Configuration .. 61

7. Conclusions 63

References 67

Appendix 73

Distribution 82

List of Illustrations

Page

1. Major components of the Saturn accelerator 12

2. Schematic of the Saturn diode. The diode is cylindrically symmetric about the center line. 14

3. Extraction efficiency in the forward 2π solid angle as a function of the source electron kinetic energy for 0.20-mm-thick tantalum converter foil 20

4. Average photon energy in the forward 2π solid angle as a function of the source electron kinetic energy for 0.20-mm-thick tantalum converter foil 22

5. Line radiation (K fluorescence) in the forward 2π solid angle as a function of the source electron kinetic energy for 0.20-mm-thick tantalum converter foil 23

6. Backscattered electrons as a function of the source electron kinetic energy for 0.20-mm-thick tantalum converter foil 24

7. Extraction efficiency in the forward 2π solid angle as a function of the thickness of the tantalum converter foil at source electron kinetic energies of 1.0 and 2.0 MeV 25

8. X-ray spectra in three angle bins for a source electron kinetic energy of 2.0 MeV and a 0.20-mm-thick tantalum converter foil 27

9. X-ray spectra in three angle bins for a source electron kinetic energy of 1.5 MeV and a 0.20-mm-thick tantalum converter foil 28

10. X-ray spectra in three angle bins for a source electron kinetic energy of 1.0 MeV and a 0.20-mm-thick tantalum converter foil 29

11. X-ray spectra in three angle bins for a source electron kinetic energy of 0.5 MeV and a 0.20-mm-thick tantalum converter foil 30

12. Average photon energy as a function of emission angle for the four source electron kinetic energies using a 0.20-mm tantalum converter foil 32

13. Radial energy deposition profiles in CaF_2 (TLD) calculated via the NE method at four axial planes for a source electron kinetic energy of 0.5 MeV and a 0.20-mm-thick tantalum converter foil 37

14. Radial energy deposition profiles in CaF_2 (TLD) calculated via the NE method at four axial planes for a source electron kinetic energy of 1.0 MeV and a 0.20-mm-thick tantalum converter foil 38

15. Radial energy deposition profiles in CaF_2 (TLD) calculated via the NE method at four axial planes for a source electron kinetic energy of 1.5 MeV and a 0.20-mm-thick tantalum converter foil 39

16. Radial energy deposition profiles in CaF_2 (TLD) calculated via the NE method at four axial planes for a source electron kinetic energy of 2.0 MeV and a 0.20-mm-thick tantalum converter foil 40

17. Mean energy deposition over an area of 573 cm^2 in CaF_2 (TLD) as a function of axial distance from the upstream surface of the converter foil calculated via the NE method at the four source electron kinetic energies using a 0.20-mm-thick tantalum converter foil 41

18. Extraction efficiency in the forward 2π solid angle and mean energy deposition over an area of 573 cm^2 in CaF_2 (TLD) as a function of the thickness of the tantalum converter foil calculated via the NE method at source electron kinetic energies of 1.0 and 2.0 MeV 43

19. Comparison of radial energy deposition profiles in CaF_2 (TLD) at an axial distance of 4.0 cm from the upstream surface of the converter foil calculated via the FT and NE methods for a source electron kinetic energy of 2.0 MeV and a 0.20-mm-thick tantalum converter foil 45

20. Comparison of mean energy deposition over an area of 573 cm^2 in CaF_2 (TLD) at an axial distance of 4.0 cm from the upstream surface of the converter foil as a function of the source electron kinetic energy calculated via the FT and NE methods with a 0.20-mm-thick tantalum converter foil 46

21. Comparison of mean energy deposition over an area of 573 cm^2 in CaF_2 (TLD) at an axial distance of 4.0 cm from the upstream surface of the converter foil as a function of the thickness of the tantalum converter foil calculated via the FT and NE methods for a source electron kinetic energy of 1.0 MeV 47

22. Comparison of radial energy deposition profiles in CaF_2 (TLD) and equivalent Si at an axial distance of 4.0 cm from the upstream surface of the converter foil calculated via the FT method for a source electron kinetic energy of 0.5 MeV and a 0.20-mm-thick tantalum converter foil. Also shown is the TLD profile calculated via the NE method 50

23. Comparison of radial energy deposition profiles in CaF_2 (TLD) and equivalent Si at an axial distance of 4.0 cm from the upstream surface of the converter foil calculated via the FT method for a source electron kinetic energy of 1.0 MeV and a 0.20-mm-thick tantalum converter foil. Also shown is the TLD profile calculated via the NE method 51

24. Comparison of radial energy deposition profiles in CaF_2 (TLD) and equivalent Si at an axial distance of 4.0 cm from the upstream surface of the converter foil calculated via the FT method for a source electron kinetic energy of 1.5 MeV and a 0.20-mm-thick tantalum converter foil. Also shown is the TLD profile calculated via the NE method 52

25. Comparison of radial energy deposition profiles in CaF_2 (TLD) and equivalent Si at an axial distance of 4.0 cm from the upstream surface of the converter foil calculated via the FT method for a source electron kinetic energy of 2.0 MeV and a 0.20-mm-thick tantalum converter foil. Also shown is the TLD profile calculated via the NE method 53

26. TLD-to-equivalent-Si conversion factor as a function of the source electron kinetic energy calculated via the FT method 54

27. Axial energy deposition profile through a 50-μm-thick disk of Si averaged over the full 15.0-cm-radius area, and calculated via the FT method for a source electron kinetic energy of 0.5 MeV and a 0.20-mm-thick tantalum converter foil -- the front surface of the disk is 4.0 cm from the upstream surface of the converter foil 57

28. Axial energy deposition profile through a 100-μm-thick disk of Si averaged over the full 15.0-cm-radius area, and calculated via the FT method for a source electron kinetic energy of 1.0 MeV and a 0.20-mm-thick tantalum converter foil -- the front surface of the disk is 4.0 cm from the upstream surface of the converter foil 58

29. Axial energy deposition profile through a 150-μm-thick disk of Si averaged over the full 15.0-cm-radius area, and calculated via the FT method for a source electron kinetic energy of 1.5 MeV and a 0.20-mm-thick tantalum converter foil -- the front surface of the disk is 4.0 cm from the upstream surface of the converter foil 59

30. Axial energy deposition profile through a 250-μm-thick disk of Si averaged over the full 15.0-cm-radius area, and calculated via the FT method for a source electron kinetic energy of 2.0 MeV and a 0.20-mm-thick tantalum converter foil -- the front surface of the disk is 4.0 cm from the upstream surface of the converter foil 60

1. Introduction

Along with HERMES III,[1] Saturn[2-4] is one of two major facilities constructed as part of the Simulation Technology Laboratory project. When completed, it will rank among the world's most powerful simulators of the X-ray effects of nuclear devices. The performance goal of Saturn is to provide a uniform X-ray exposure capability of 5×10^{12} rad(Si)/s over an area of 500 cm^2. This would make Saturn a unique facility for subsystem and system testing and would represent a significant advance in above ground testing technology.

The Saturn project involves the conversion of the PBFA-I ion accelerator[5] into an X-ray simulator that will meet these goals. At a minimum, a 25-TW, 500-kJ relativistic electron beam (i. e., nominally 12.5 MA of 2.0 MeV electrons for 20 ns) must be delivered to a tantalum converter/anode with a suitable phase space distribution to meet these requirements. This has necessitated significant upgrade in the energy storage and pulse forming sections of PBFA-I, as well as the design and construction of a power flow section, diode, and converter to efficiently utilize the available pulsed power. The major components of Saturn are shown in Fig. 1. This report is concerned with the prediction of the more critical aspects of the radiation environment for the expected performance of the baseline diode design.

In Secs. 2 and 3, we describe the baseline diode and discuss the calculational model that has been used to predict the radiation environment. The expected X-ray extraction efficiency and the X-ray spectrum are

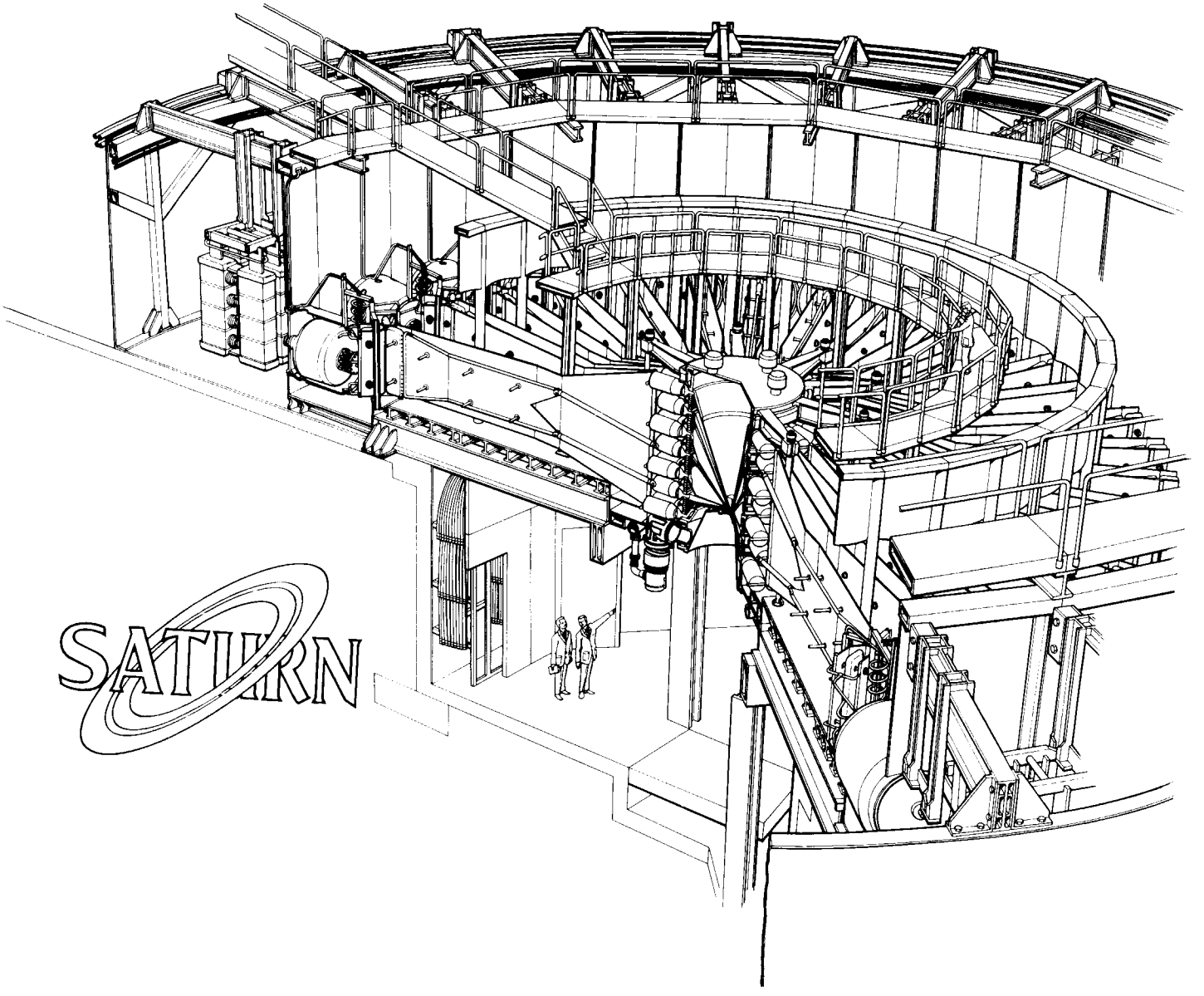

Fig. 1. Major components of the Saturn accelerator.

presented in Sec. 4. Section 5 deals directly with the Saturn design goals with a discussion of the predictions of the near-field energy deposition profiles in Si and thermoluminescent dosimetry (TLD). In Sec. 6, we discuss predictions of the primary electron deposition in the converter system, which may be useful in addressing such issues as thermomechanical response and ion formation.

2. Description of the Saturn Baseline Diode

The Saturn baseline diode is shown in Fig. 2. The diode is modular, consisting of three concentric triaxial diodes.[6,7] It is called a 3-ring diode because of the three cathode rings. Each triaxial diode is electrically isolated from the others and produces an annular electron beam. The linear current density is the same for each ring (~90 kA/cm), with 1/6 of the accelerator current driving the inner ring, 1/3 the middle ring, and 1/2 the outer ring. The inner cathode ring extends from 3.0 to 4.0 cm, the middle ring from 7.5 to 8.5 cm, and the outer ring from 11.0 to 12.0 cm. The beam electrons are injected into a 0.20-mm-thick tantalum anode/converter which is optimized for converting electron energy into radiation. Electrons that are transmitted through the anode are absorbed in a 4.8-mm-thick graphite (1.76 g/cm^3) beam stop. The purpose of the beam stop is to prevent excessive energy deposition in the 1.3-cm-thick Kevlar debris shield which is needed to protect downstream test objects from debris.[8] The graphite and Kevlar materials also were chosen for their low attenuation of X rays.

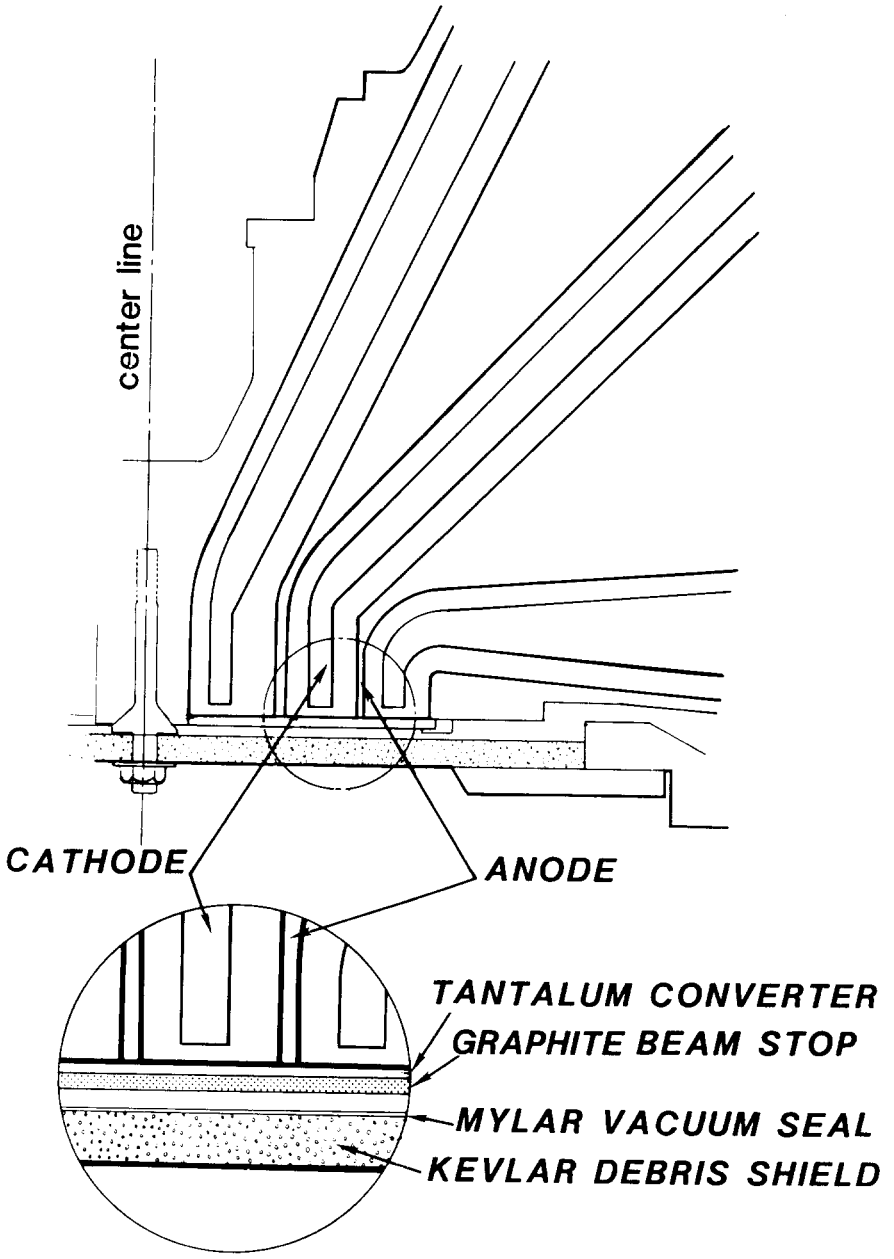

Fig. 2. Schematic of the Saturn diode. The diode is cylindrically symmetric about the center line.

The modular design of the diode is essential to obtaining a uniform radiation environment close to the converter. It allows the diode to operate at a very low impedance (nominally 0.16 Ω), and it reduces the inductance of the vacuum section by about 50% from what would be possible with a single-element diode. Ion current can be a significant loss in a low-impedance electron diode, but the triaxial geometry limits the ion current to a few percent of the diode current. Triaxial diodes have proven to be very reliable on Proto II, SPEED, and Hydramite[6,7] provided that the power pulses on the inner and outer sides of the triaxial feed are balanced and that the accelerator prepulse is not too large. Great care was taken in designing Saturn to insure these conditions. The triaxial geometry also is compatible with a scheme to transport an electron beam by gradient-B drift in an applied magnetic field.[9,10]

Under nominal operating conditions, the maximum kinetic energy of the beam electrons is expected to be about 2.0 MeV. For radiation effects experiments that are very sensitive to the X-ray energy spectrum, it is desirable to reduce the peak diode voltage.[11] Reducing the anode-cathode gap will cause the diode to operate at an impedance less than the accelerator impedance, which will increase the current and decrease the voltage.[12] In this case, the thicknesses of the anode and beam stop should also be reduced to increase the extracted X-ray energy.

3. Description of the Calculational Model

The radiation transport calculations are based upon primary electron source distributions defined at the anode plane. PIC-code (particle-in-cell code) calculations were made to predict the diode impedance.[13] However, the primary electron distributions at the anode were not obtained in these simulations. Being thus forced to make assumptions about these distributions, we have made rather simple choices. In all calculations, the electrons were monoenergetic and normally incident on the Ta converter foil. Spatially, the electrons were assumed to be distributed uniformly over each of three rings at the anode surface with precisely the same dimensions as the cathode rings. The fraction of the source within each ring was proportional to the number of modules driving the corresponding cathode ring.

The azimuthal symmetry of the source led quite naturally to our choice of the CYLTRAN code of the ITS system[14] as the basis of the calculational model. However, CYLTRAN has an important limitation. At source electron energies expected for the Saturn facility, the reflection coefficient for Ta is quite high.[15] Electrons that are reflected from the anode converter foil in the Saturn diode will find themselves in the accelerating field of the diode which cannot be modeled by CYLTRAN. One alternative would be to approximate some quasi-steady state electric and magnetic diode fields as externally applied fields in the CYLTRANM code.[14,16] But these fields can only be determined from self-consistent PIC-code calculations that themselves properly account for the collisional backscatter from the anode. No such PIC code presently exists. Another approach that has been used in

the past would be to assume localized specular reflection at the reflection surface of the converter foil, thus reinjecting the otherwise collisionally reflected electrons. This would lead to an overestimate of the X-ray production.[16] We have taken the conservative approach of simply allowing the reflected electrons to escape, which should result in lower bounds for the calculated X-ray environments.

The X-ray source region, the converter system or converter configuration, where the beam electrons convert a small percentage of their energy to radiation is modeled as a series of five coaxial disks having radii of 15.0 cm. The thicknesses, in sequence, are as follows:

(1) Variable thickness tantalum converter foil
(2) 0.48 cm graphite electron absorber (mass density = 1.76 g/cm^3)
(3) 0.40 cm void
(4) 0.025 cm Mylar vacuum seal
(5) 1.27 cm Kevlar debris shield

One of the more important objectives of this study was to investigate the dependence of various aspects of the X-ray environment on the thickness of the converter foil. Where dosimetry/detector response was desired, the relevant additions to this source-region configurations were included using either the more approximate, but more efficient, next-event-estimator (NE) method or the more accurate, but slower, full-transport (FT) technique. These approaches are discussed in more detail below.

The nominal mean electron kinetic energy of the electron spectrum generated in the Saturn diode is expected to be between 1.5 and 2.0 MeV. Experience tells us, however, that there will be a significant spread in the energies of source electrons contributing to the X-ray production. Moreover, there will be some demand for operation at lower voltages to obtain softer spectra. Consequently, we have studied the environments at 0.5, 1.0, 1.5, and 2.0 MeV.

4. X-Ray Output

Using the converter configuration described in the previous section, the CYLTRAN code was used to predict the extracted X-ray efficiency and the singly and doubly differential distributions of those X rays.

The predictions of the X-ray output described in the previous subsection represent a special capability of the TIGER and CYLTRAN codes of the ITS system.[14] These predictions involve transport only in the converter system, and they are concerned only with the production of X rays and a prediction of the escape of those X rays from the converter configuration. Even though the conversion efficiency of electrons at Saturn source energies is small, two variance-reduction options are available that make such calculations extremely efficient. The first of these is a scaling of the X-ray production cross section that leads to the generation of X rays in quantities well above their natural populations. The second is an estimator of photon escape (default in the CYLTRAN code) that does not depend on actual transport across the escape boundary. Rather, this estimator --

called the next-event-estimator -- results in a contribution to the photon escape at each collision from which a photon emerges; the quantity that is scored is simply the weight of the emerging photon times the probability that it will escape without further interaction. These two standard options permit the rapid prediction of accurate photon escape distributions by minimizing the number of source electron histories that would otherwise be required.

4.1 X-Ray Extraction Efficiency

It is expected that the mean source electron kinetic energy at the Saturn anode will be somewhere between 1.5 and 2.0 MeV under nominal operating conditions. From past experience with other accelerators operating in this energy range, we assume that the optimum thickness of the Ta converter foil will be about 0.20 mm. Using this value with the converter configuration defined in Sec. 3, we obtain the results shown in Fig. 3 for the X-ray extraction efficiency in the forward 2π solid angle as a function of electron energy. Here and elsewhere, the smooth curves are not fits, but rather interpolants through the data points, and the error bars are the estimated one-sigma statistical uncertainties. Thus, under nominal conditions, we would expect that about 2% of the beam energy, or 10 kJ, should be available for the simulation of X-ray effects. Figure 3 also provides an indication of the penalty to be paid for operating the facility at lower operating voltages. Of course, some improvement over these efficiencies can be expected from converter configurations that are

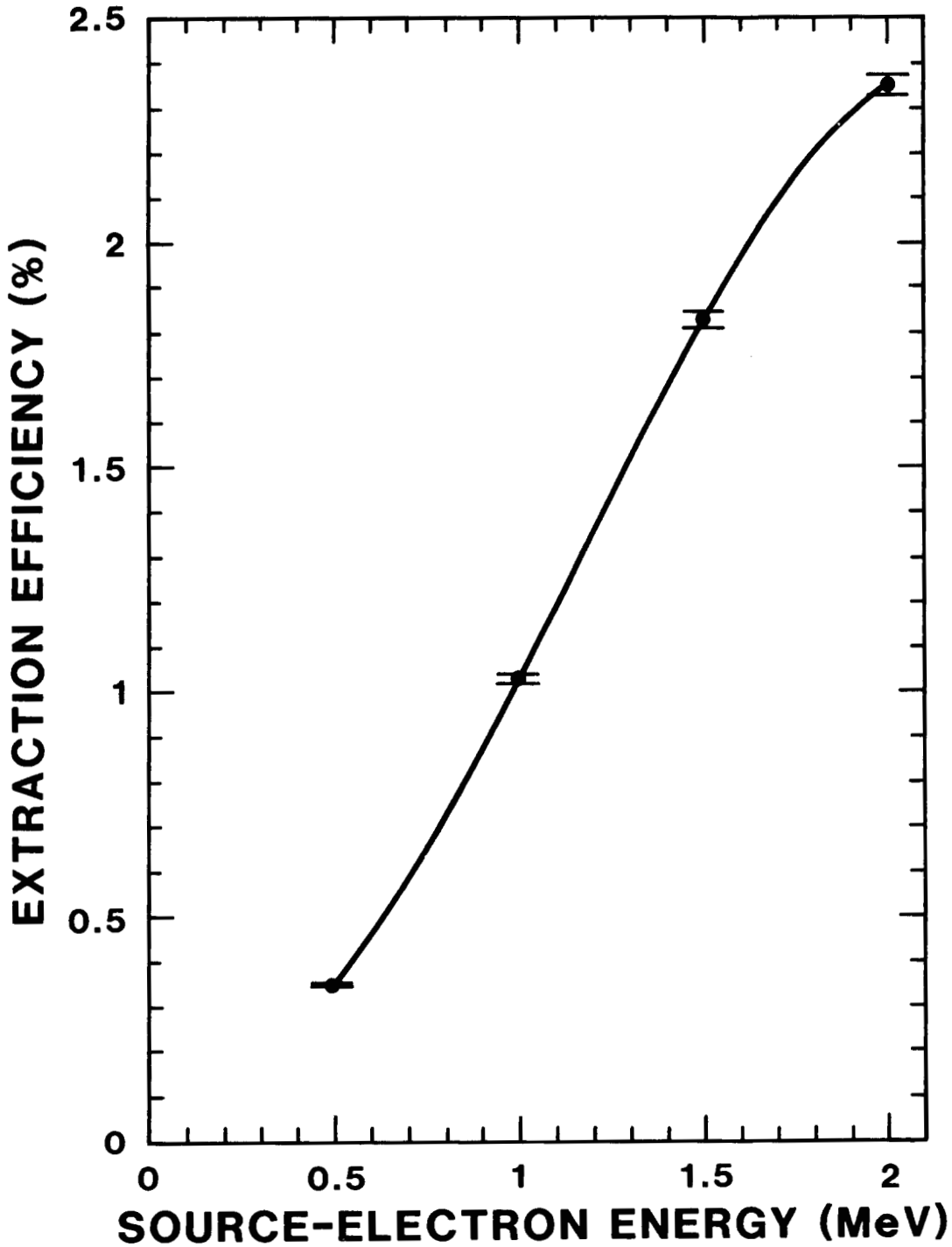

Fig. 3. Extraction efficiency in the forward 2π solid angle as a function of the source electron kinetic energy for 0.20-mm-thick tantalum converter foil.

optimized for a particular X-ray effects experiment (see e. g., Sec. 5 and Fig. 4 of Ref. 17).[17-19]

Other aspects of the electron energy dependence of this converter configuration are shown in Figs. 4, 5, and 6. Figure 4 shows the average photon energy as a function of electron energy. This quantity is of very limited usefulness because of the strong dependence of X-ray effects on photon energy. Indeed, it is possible to define an effective energy for a particular X-ray response that better characterizes the fidelity of the simulation of a particular radiation effect or response.[20] The detailed spectra will be discussed in Sec. 4.2. One feature that is unique to X-ray spectra in this energy range is the prominence of K-fluorescent line radiation from the Ta converter foil. Figure 5 shows the percentage of the extracted X-ray energy that is contained in this line radiation. The electron albedo is plotted in Fig. 6 as a function of electron energy. A portion of the radiation that would otherwise have been produced by these electrons may be recovered through reinjection by the electric field of the diode. Because these electrons are reflected from a high-Z converter foil, they are quite energetic.[15] Consequently, the recovered X-ray energy may be significant.[16]

Electron beams obtained from Marx-generator based pulsed power technology typically have rather broad spectra.[21] In the absence of reliable predictions of the Saturn spectrum, the choice of 0.20 mm for the thickness of the Ta foil in Figs. 3-6 was an educated guess at the optimum. Figure 7 shows the dependence of the extraction efficiencies at source electron energies of 1.0 and 2.0 MeV on the Ta thickness when the rest of

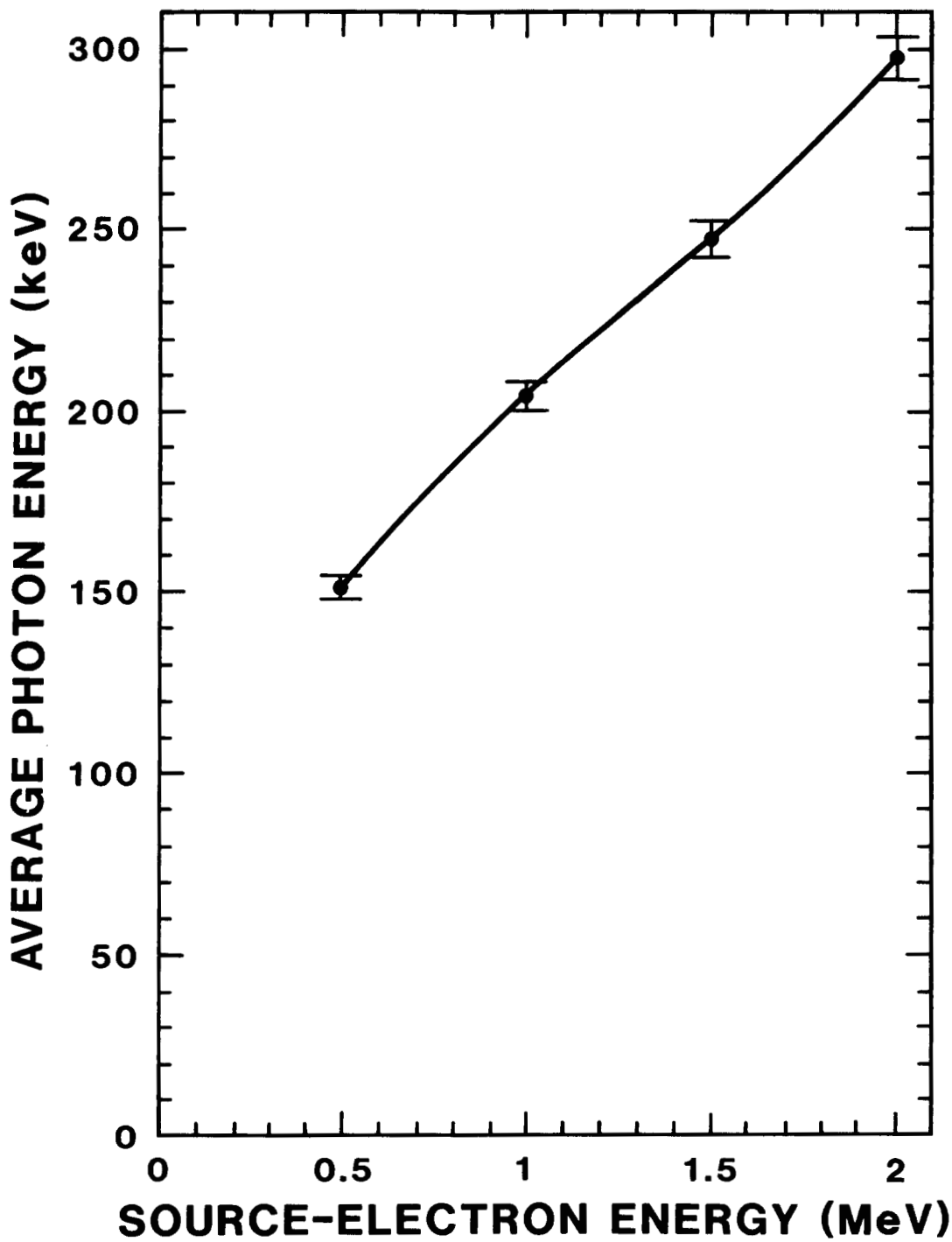

Fig. 4. Average photon energy in the forward 2π solid angle as a function of the source electron kinetic energy for 0.20-mm-thick tantalum converter foil.

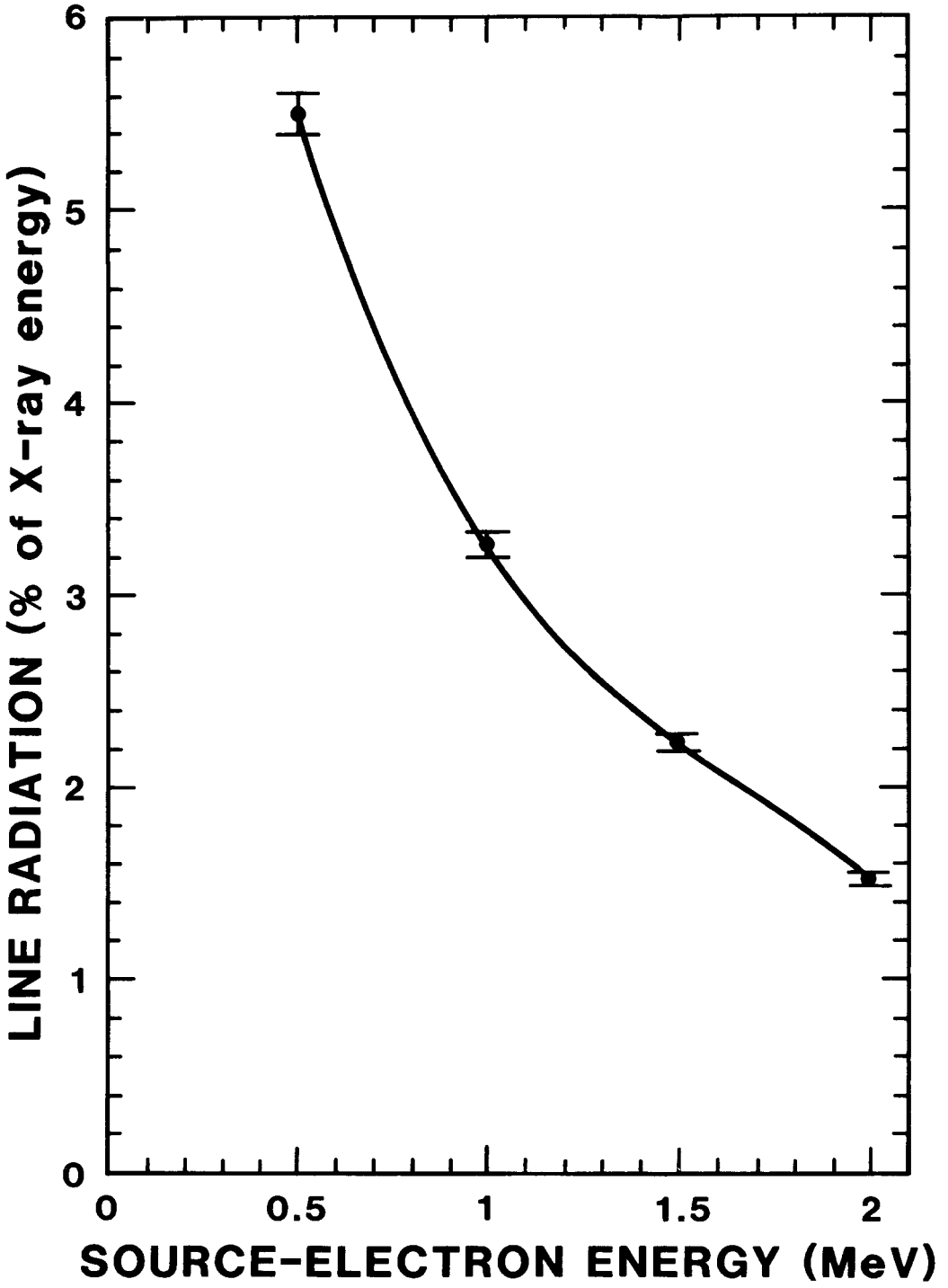

Fig. 5. Line radiation (K fluorescence) in the forward 2π solid angle as a function of the source electron kinetic energy for 0.20-mm-thick tantalum converter foil.

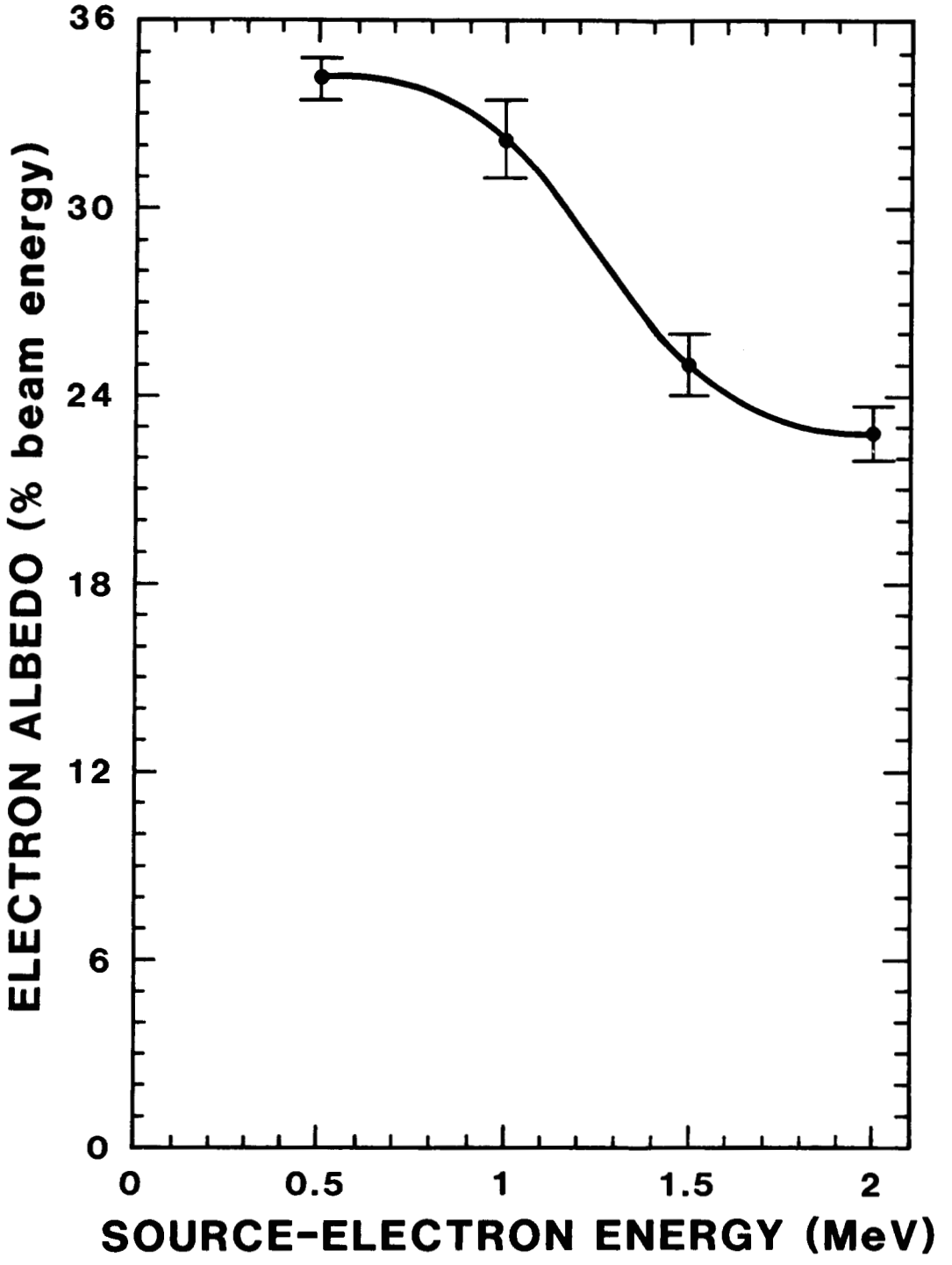

Fig. 6. Backscattered electrons as a function of the source electron kinetic energy for 0.20-mm-thick tantalum converter foil.

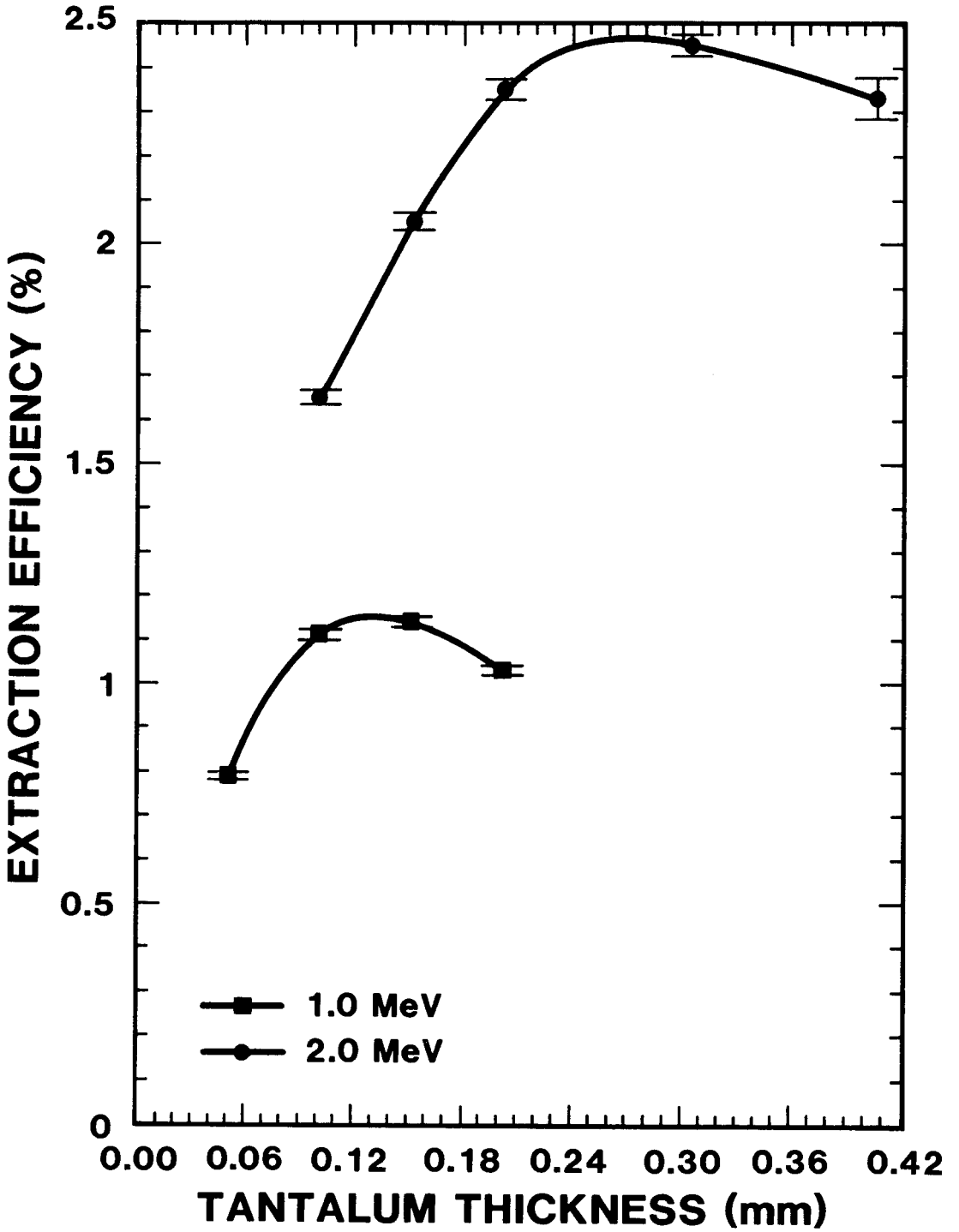

Fig. 7. Extraction efficiency in the forward 2π solid angle as a function of the thickness of the tantalum converter foil at source electron kinetic energies of 1.0 and 2.0 MeV.

the converter configuration is fixed as described in Sec. 3. According to these results, the electron energy at which this configuration would maximize the extraction efficiency lies somewhere between 1.0 and 2.0 MeV, thus confirming that the 0.20-mm foil thickness was a reasonable choice.

4.2 Differential X-Ray Distributions

A detailed analysis of the response of experiments to X rays in this energy region can only be carried out with some knowledge of the X-ray spectrum. The ultimate assessment of the fidelity of the simulation will depend on such an analysis. Furthermore, because most exposures will be in the near field, the variation in the spectrum with emission angle is also useful.

The calculated spectra are shown in order of decreasing source electron energy in Figs. 8-11. At each energy, the spectra are shown for three angular intervals with 0° being straight ahead. Except where the spectra fall off at high and low photon energies, the estimated one-sigma statistical uncertainties are usually better than 10% in the 0-10° angle bin and better than 5% in the two higher angle bins. The most prominent features of the spectra are the Ta K-fluorescent lines (1 keV bins) at a mean energy of about 59 keV and the depression just above the line energy corresponding to the K-shell absorption edge (binding energy) of Ta. There is some concern that when the Saturn accelerator is operated at the nominal energy, the spectrum will be too hard for some simulations.[11] On the other hand, it can be shown that many experiments are transparent to the

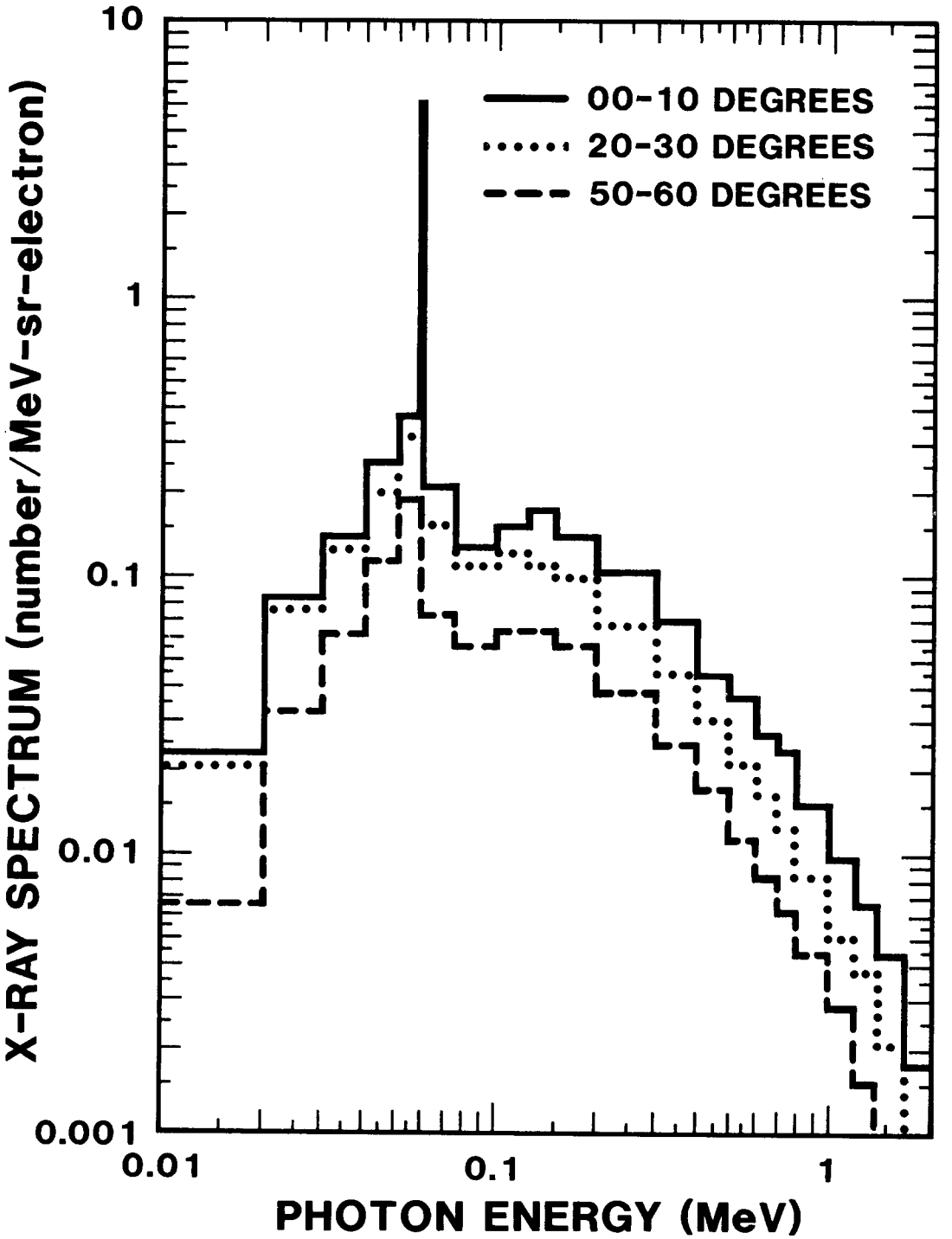

Fig. 8. X-ray spectra in three angle bins for a source electron kinetic energy of 2.0 MeV and a 0.20-mm-thick tantalum converter foil.

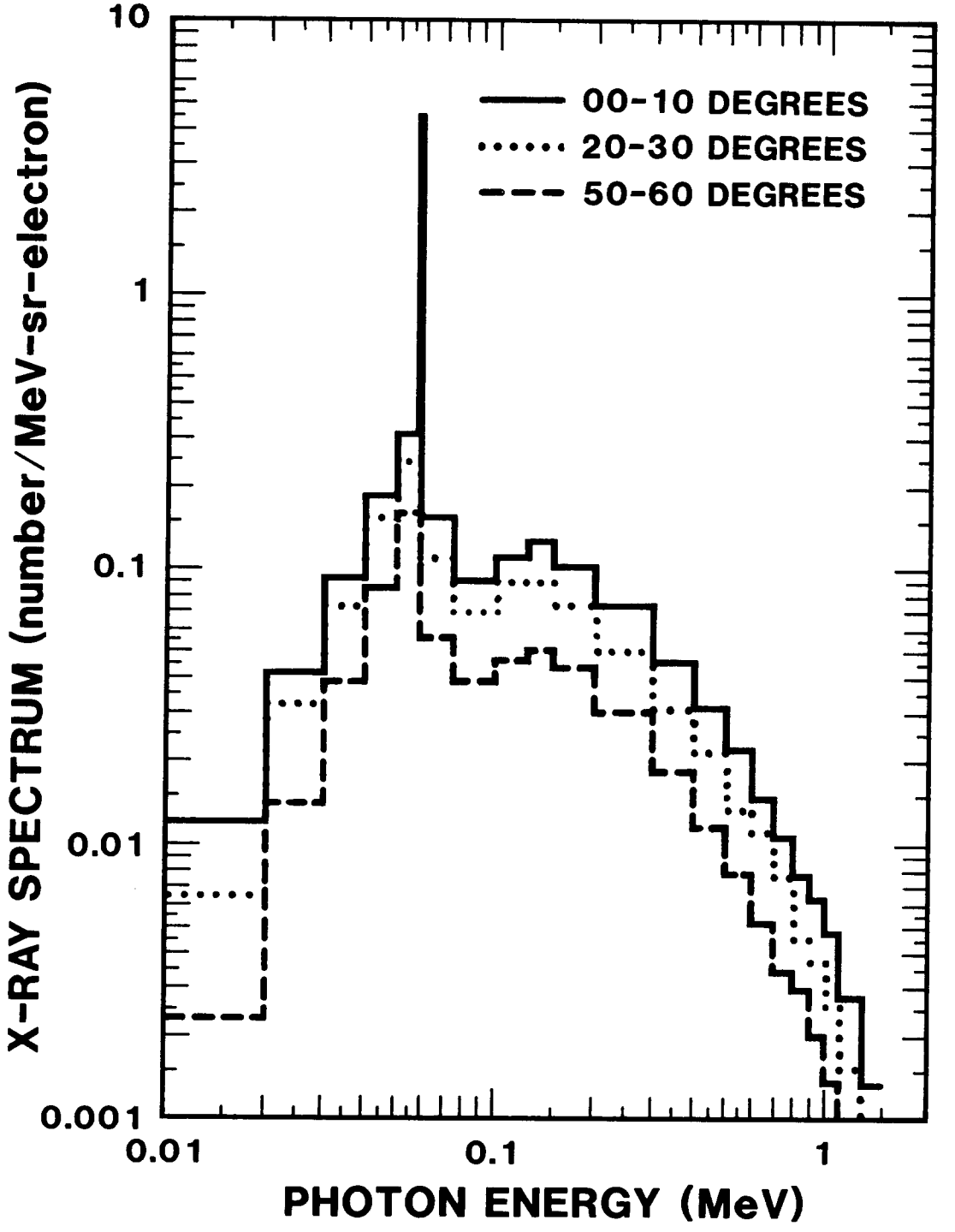

Fig. 9. X-ray spectra in three angle bins for a source electron kinetic energy of 1.5 MeV and a 0.20-mm-thick tantalum converter foil.

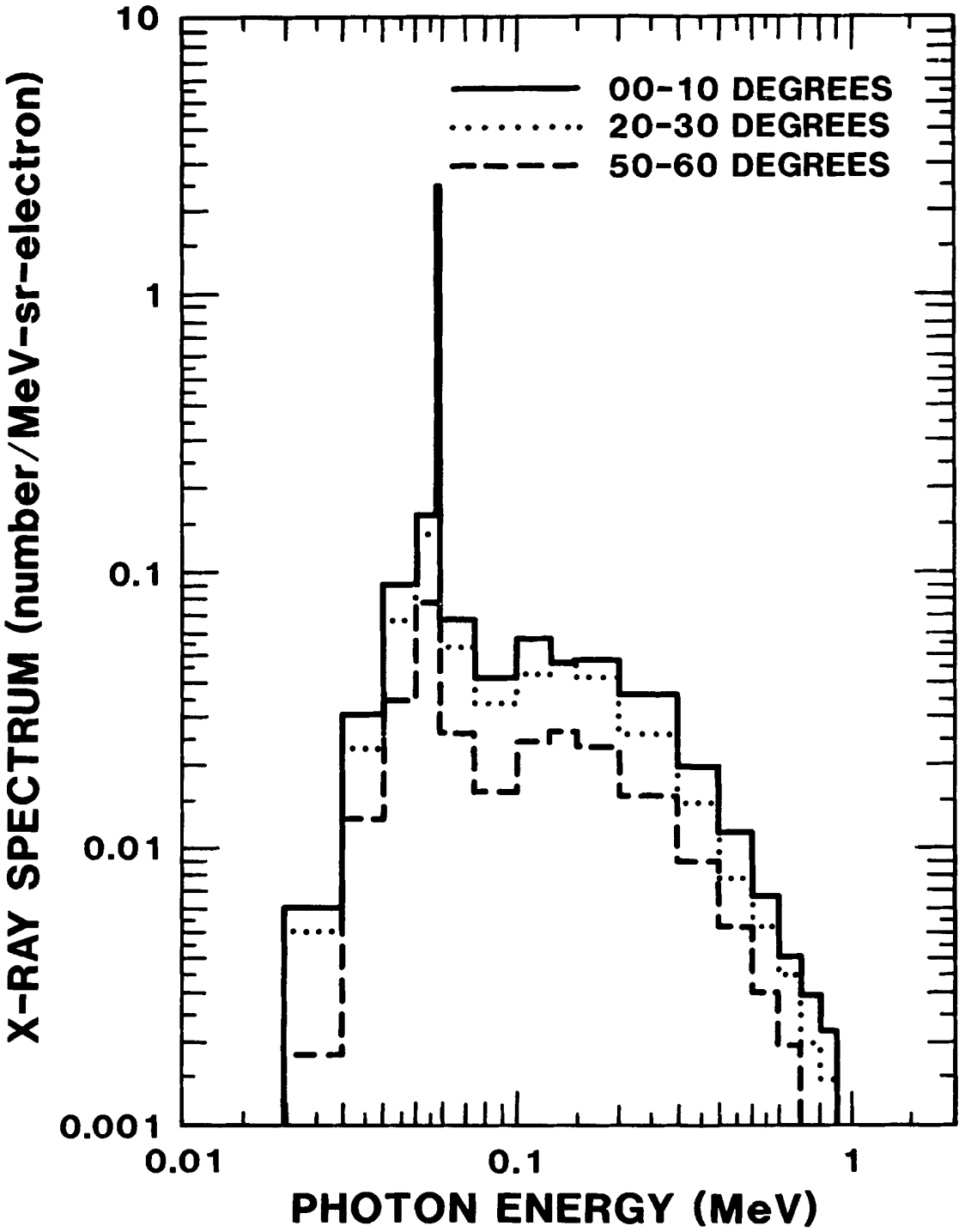

Fig. 10. X-ray spectra in three angle bins for a source electron kinetic energy of 1.0 MeV and a 0.20-mm-thick tantalum converter foil.

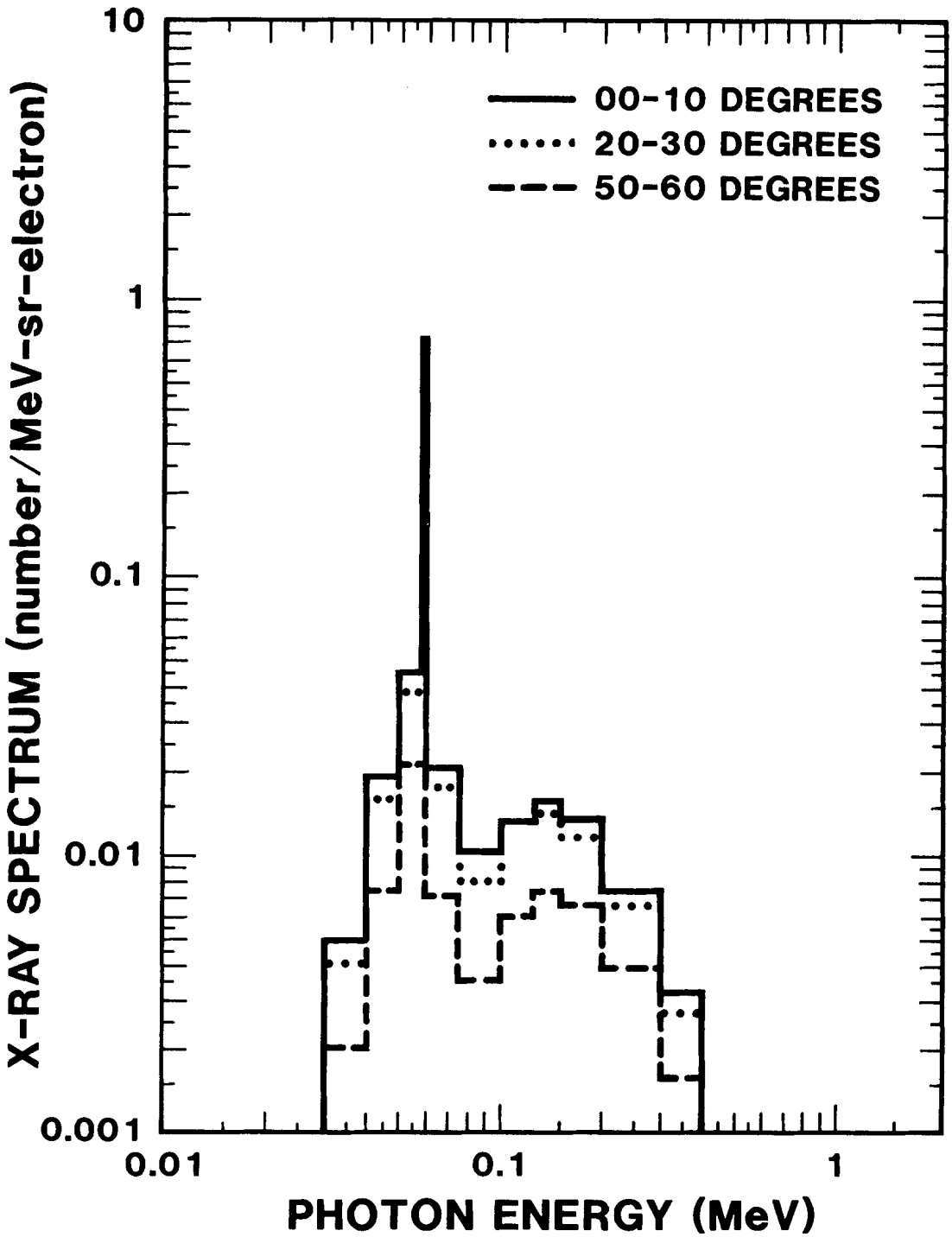

Fig. 11. X-ray spectra in three angle bins for a source electron kinetic energy of 0.5 MeV and a 0.20-mm-thick tantalum converter foil.

high-energy tail of the simulation spectra so that this tail is not important.[20] Nevertheless, flexibility in the design of the facility will allow the alternative of operating at a reduced voltage, albeit with a penalty on output efficiency as shown in Fig. 3.

It is important to note that the bremsstrahlung cross sections currently being used in the ITS system are not the best available. They are based on the Born approximation,[22,23] and the range of electron energies and the converter materials for which they are least accurate closely correspond to those of flash X-ray sources used for X-ray simulation. Interestingly enough, however, when measurements of the response of Au calorimetry[24] and Ta wrapped CaF_2 TLDs[25] were compared with calculations based on both the Born-approximation cross sections and improved cross sections,[26] little difference in the predictions was seen. Still, while the predicted responses were not very sensitive to the cross sections used, the calculated thick-target bremsstrahlung output spectra were much more so,[24] suggesting that there were compensating effects in these particular integral responses which masked the effects of the spectral differences.

The spectra in Figs. 8-11 do not appear to change much with angle. In Fig. 12, we have plotted the average photon energy as a function of emission angle for the four source energies. The estimated one-sigma statistical uncertainties are usually less than or equal to 3%. These results are quite different from those in Figs. 13a-c of Ref. 19. In the latter case, the spectra were always harder at the highest angles of emission. While some of the differences are no doubt due to the fact that the converters are not as carefully optimized in the present work, the much softer spectra in the

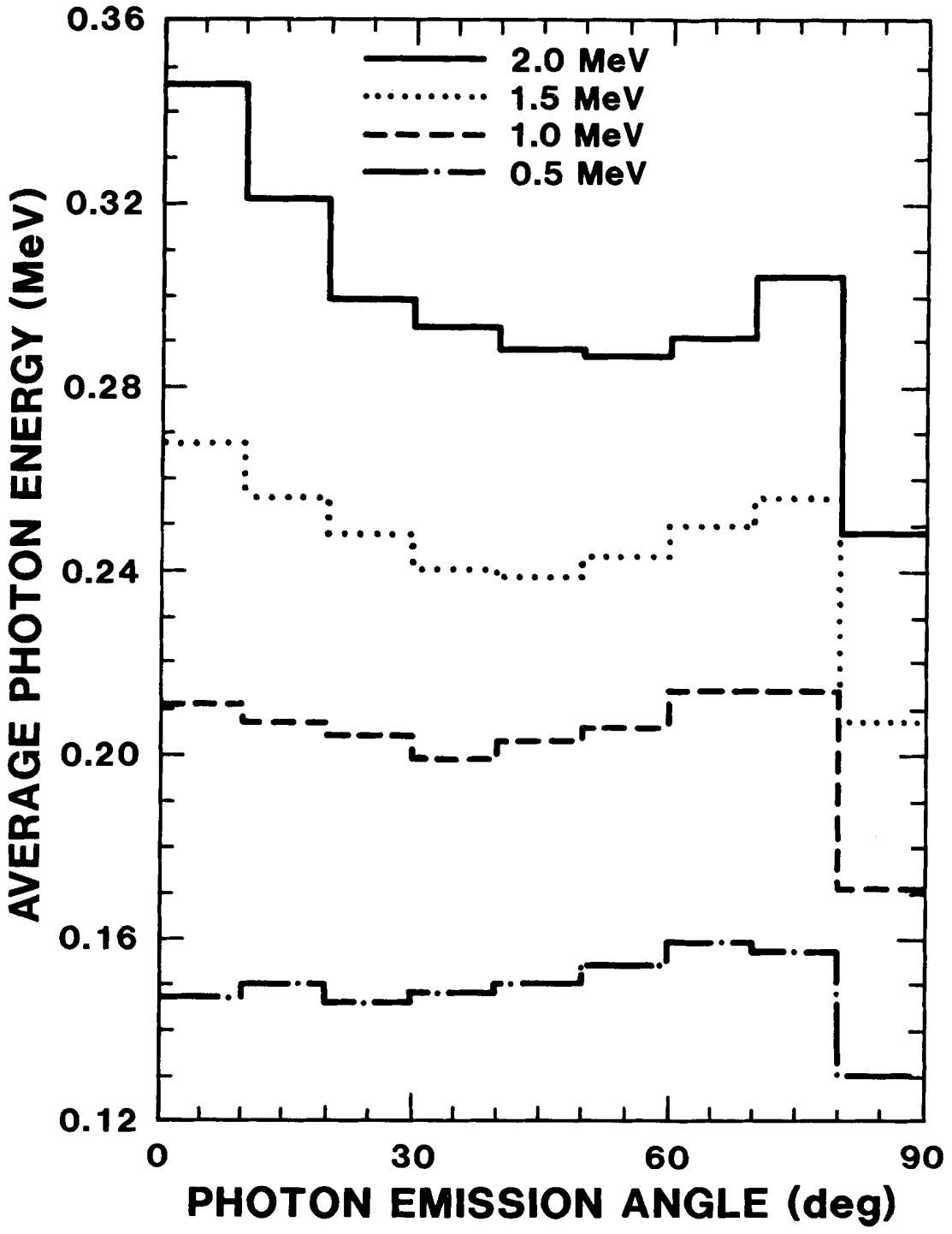

Fig. 12. Average photon energy as a function of emission angle for the four source electron kinetic energies using a 0.20-mm tantalum converter foil.

80°-90° interval of Fig. 12 is believed to be a two-dimensional effect. Much of the high-energy, high-angle radiation generated in the Ta converter foil that was eventually transmitted in the one-dimensional geometry employed in Ref. 19 does not escape through the downstream face of the Kevlar debris shield in the present work. Only this latter radiation is included in the results of Figs. 3-12. What this means is that the high angle emission may be very sensitive to details of the experimental converter configuration and surrounding support structure, and is coupled to the spatial distribution of the emitted X rays. This behavior indicates the complexity of the radiation fields of X-ray and γ-ray simulators that may be expected for close-in exposures.

5. X-Ray Energy Deposition

While information on the extracted X rays is useful, it is of limited practical value for flash X-ray sources because it is not directly measurable and is not specified in the design criteria of the machine. What is measured is the integral over photon energy of the response of some detector/dosimeter, or some component or subsystem, to the X rays. Moreover, what is ultimately desired in the way of prediction is the "X-ray energy deposition" in some target geometry, or simply the deposition to be expected in some critical material such as Si.

If the deposition in these "X-ray targets" is significantly affected by a lack of electron equilibrium, we have no choice but to include full transport of the electron/photon cascade in this region, along with the

converter configuration described in Sec. 3. Such combined, or full transport (FT), calculations of X-ray production and X-ray response have only recently become practicable.[27] Even then, they can be quite expensive. In an attempt to avoid this difficulty, the production and response calculations are often performed separately with the X-ray output of the former used as the source for the latter. The problem with this approach is that in the response calculations it is virtually impossible to accurately account for the strong coupling between the spatial, angular, and energy distributions of the source X rays that obtains in the near-field geometries that concern us here.

For a certain class of near-field problems, where there is good electron equilibration in the detector and where buildup of secondary photons within the detector itself is not important, we use an alternative to the FT method that is much faster than that method, while accurately accounting for the coupled phase-space distribution of the X rays escaping the converter region. This alternative is hereafter referred to as the next-event-estimator (NE) method. It is an extension to the prediction of energy deposition of the next-event-estimator described above for X-ray extraction.

A more detailed discussion of the FT and NE methods can be found in the appendix. Further discussion and comparisons of the predictions of the two methods can be found in Ref. 27. The remainder of this section is concerned with the results of calculated energy deposition profiles for the CaF_2 TLD material and Si that were obtained using one or both of these methods.

5.1 Thermoluminescent Dosimetry

CaF_2 thermoluminescent dosimetry is our most routine flash-X-ray diagnostic. The 3.2-mm-square, 0.89-mm-thick active material is most frequently encapsulated between 0.22-cm (upstream) and 0.23-cm (downstream) of Al. The results of Refs. 17, 28, and 29 confirm the capability of the ITS model, combined with the procedures described in the appendix of this document, for accurately predicting energy deposition in these TLDs by X rays generated with well defined electron sources in this energy range. Even though these equilibration thicknesses are excessive, we expect that convenience will dictate their use. All TLD predictions in this report assume this configuration. The unnecessarily high attenuation by the 0.22-cm of Al means that our predictions of the bulk energy deposition in CaF_2 may be lower bounds to what can actually be achieved.

5.1.1 The NE Method --- The results in Ref. 27 lead us to expect that the NE method will underpredict the TLD deposition by about 25%. Nevertheless, the considerable advantages of the method lead us to use it here. Its power lies both in its efficiency for calculating a particular output and in the fact that it permits the calculation of an arbitrary number of different outputs within a single Monte Carlo run that would otherwise necessitate separate runs. Thus, for each converter configuration and source energy, we have obtained radial energy deposition profiles in the TLDs at four axial planes downstream of the converter from a single run. Moreover, since the Monte Carlo transport is restricted to the converter configuration alone, the X-ray output results of the previous section were obtained simultaneously.

The four axial planes were defined in such a way that the upstream surface of the CaF_2 was 2.5, 4.0, 5.0, and 10.0 cm downstream of the upstream surface of the Ta converter foil (the source plane). At each plane, an array of TLDs was simulated by a quasi-one-dimensional configuration consisting of five 15.0-cm-radius coaxial disks in the following upstream-to-downstream order: 0.51 mm Lucite, 0.22 cm Al, 0.89 mm CaF_2, 0.23 cm Al, and 0.51 mm Lucite. The Lucite simulates a wrapper that is employed for convenience in handling, but represents additional unnecessary attenuation of the X rays.

The radial profiles at the four axial distances obtained with the NE method are plotted in Figs. 13-16 for each of the four source energies. The estimated one-sigma statistical uncertainties are usually less than 5%. At an axial distance of 2.5 cm, the ring structure of the electron source is still evident. However, in none of the profiles does the dose vary by more than a factor of two within a radius of 13.5 cm (573-cm^2 area). Absolute estimates can be obtained by assuming that some number of coulombs per pulse will be realized at a particular effective source energy. For example, if we assume a value of 0.25 C/pulse (12.5 MA for 20 ns) at an effective energy of 2.0 MeV, the peak deposition in Fig. 16 would be about 1.4×10^5 rad. Correspondingly, a peak current of 12.5 MA at an effective energy of 2.0 MeV would yield a peak dose rate of about 6.8×10^{12} rad/s. For an effective energy of 0.5 MeV at the same peak current, the peak dose rate would drop to about 3.5×10^{11} rad/s.

The mean dose over a 573-cm^2 area is plotted in Fig. 17 as a function of axial distance. Absolute mean depositions and deposition rates can be

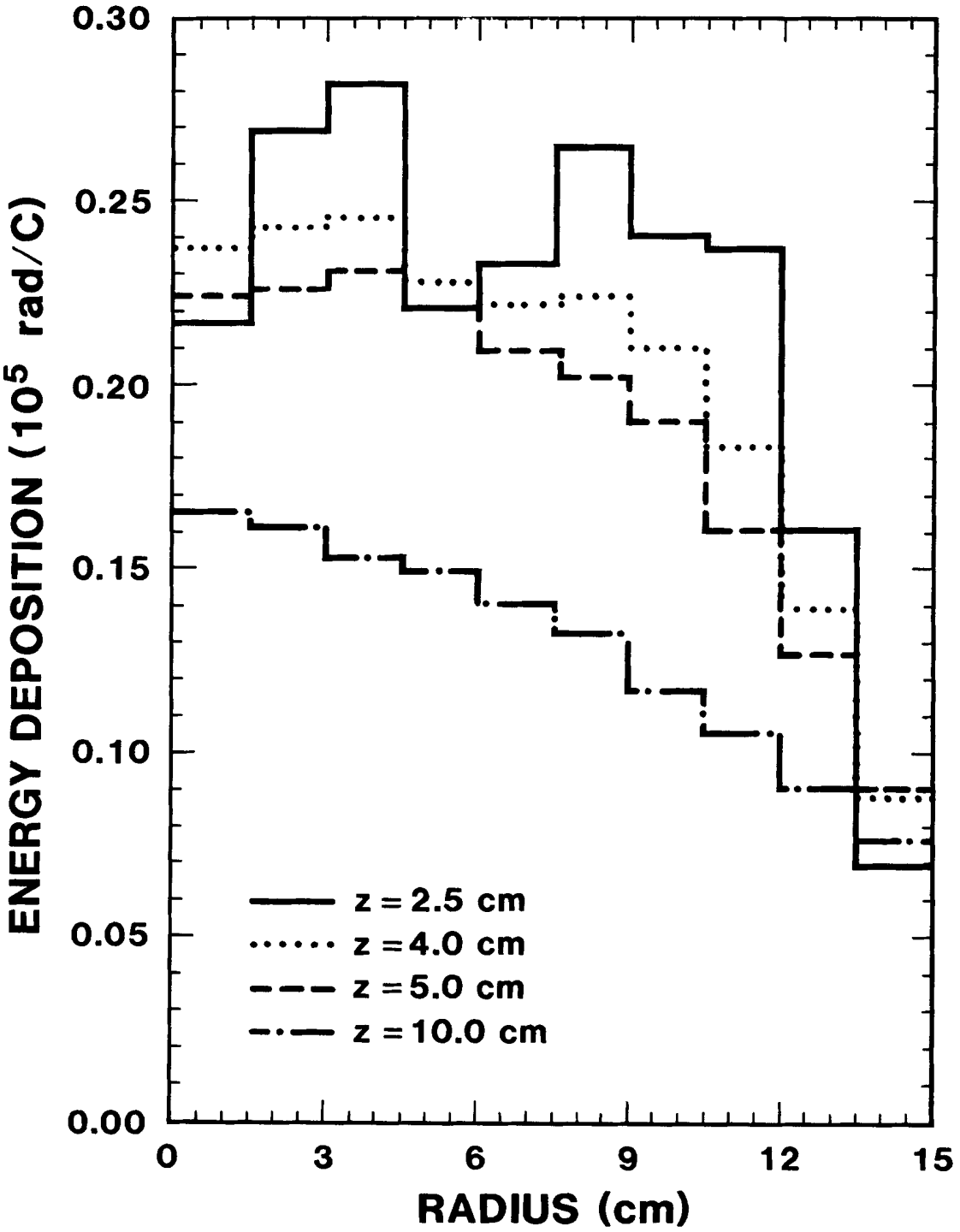

Fig. 13. Radial energy deposition profiles in CaF_2 (TLD) calculated via the NE method at four axial planes for a source electron kinetic energy of 0.5 MeV and a 0.20-mm-thick tantalum converter foil.

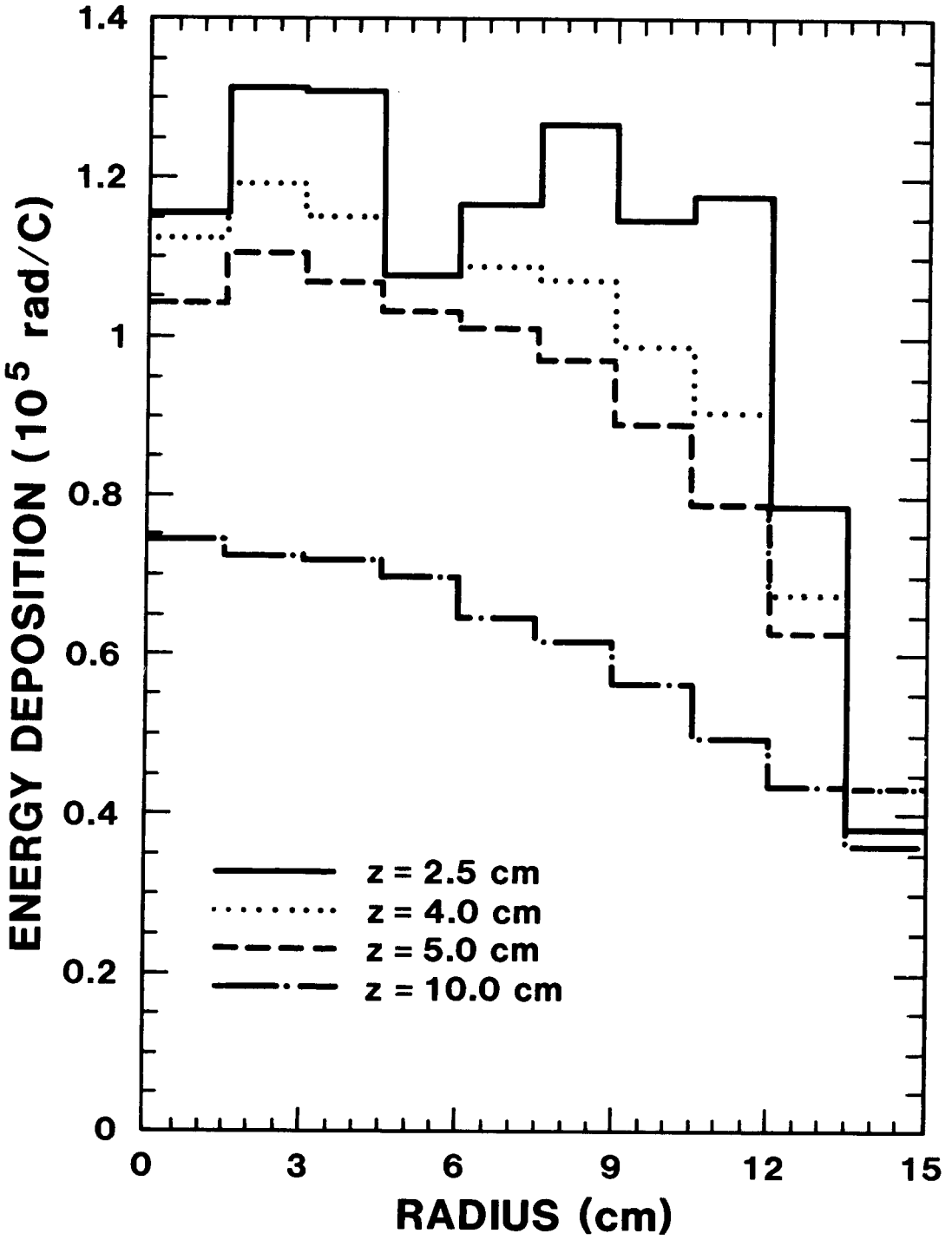

Fig. 14. Radial energy deposition profiles in CaF_2 (TLD) calculated via the NE method at four axial planes for a source electron kinetic energy of 1.0 MeV and a 0.20-mm-thick tantalum converter foil.

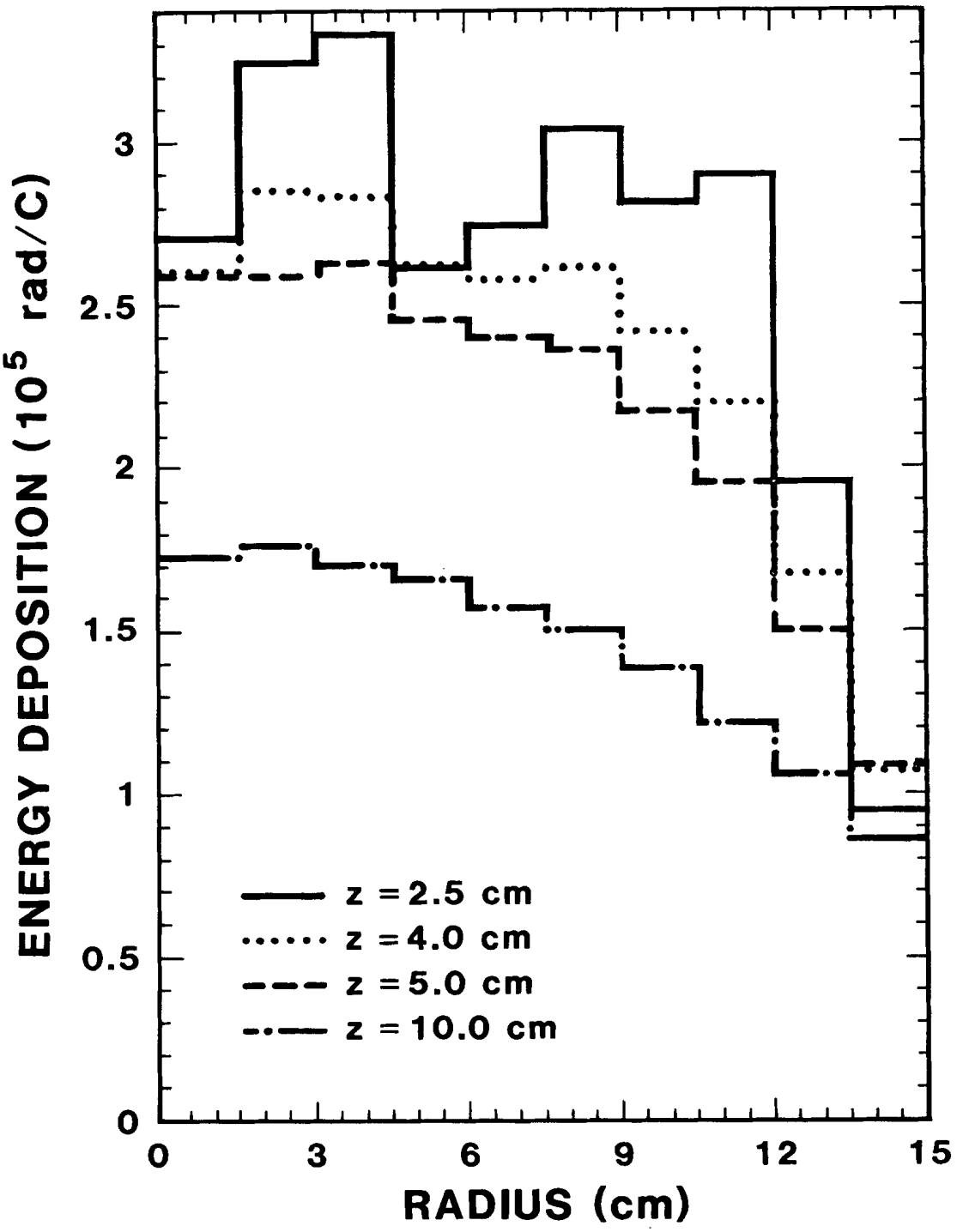

Fig. 15. Radial energy deposition profiles in CaF_2 (TLD) calculated via the NE method at four axial planes for a source electron kinetic energy of 1.5 MeV and a 0.20-mm-thick tantalum converter foil.

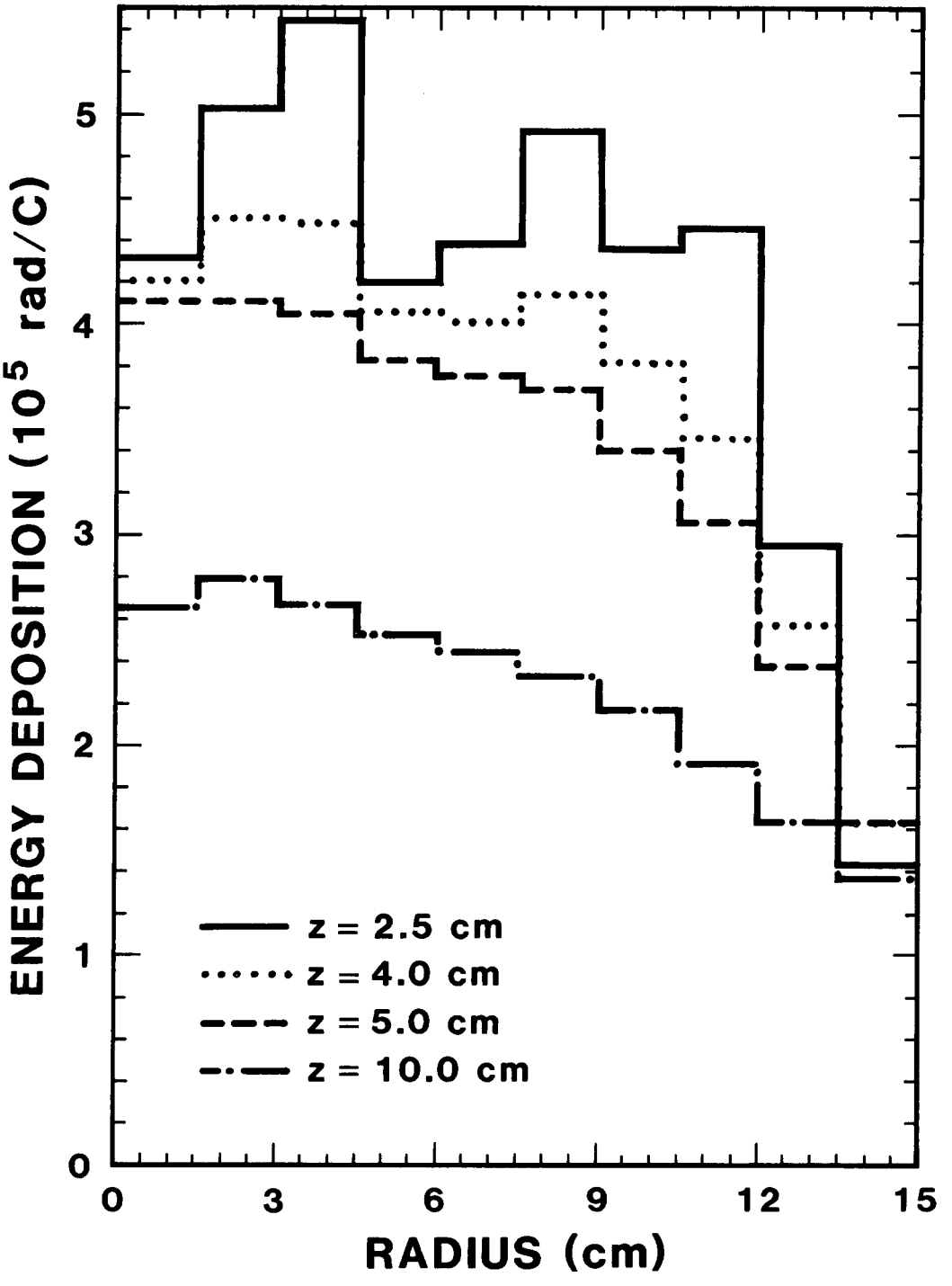

Fig. 16. Radial energy deposition profiles in CaF_2 (TLD) calculated via the NE method at four axial planes for a source electron kinetic energy of 2.0 MeV and a 0.20-mm-thick tantalum converter foil.

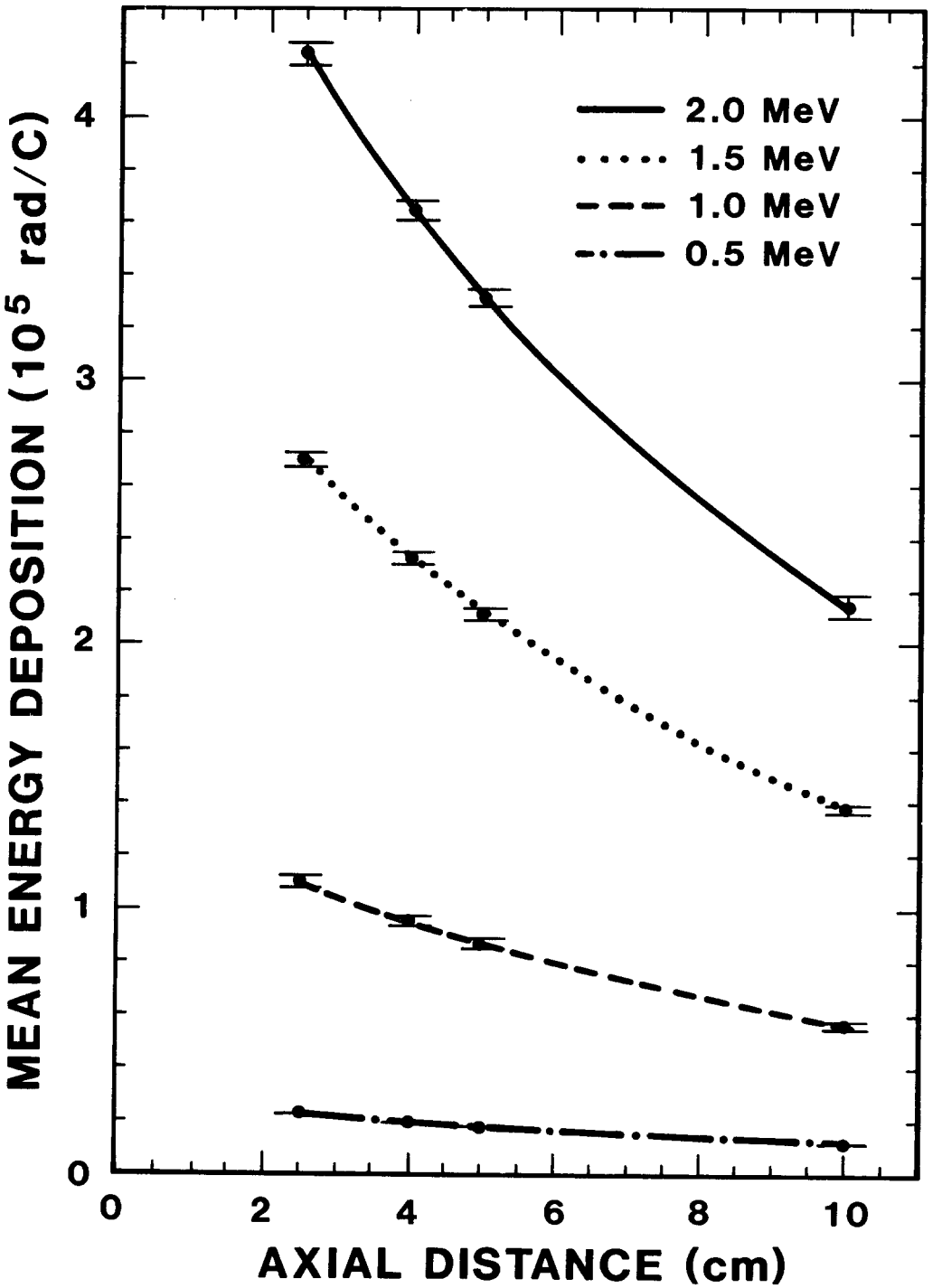

Fig. 17. Mean energy deposition over an area of 573 cm^2 in CaF_2 (TLD) as a function of axial distance from the upstream surface of the converter foil calculated via the NE method at the four source electron kinetic energies using a 0.20-mm-thick tantalum converter foil.

estimated by making appropriate assumptions as discussed in the previous paragraph. Though there is no specified axial uniformity requirement for Saturn, Fig. 17 predicts that the reduction in the mean deposition as the location of the exposure plane is increased from 2.5 to 10.0 cm will be less than a factor of two.

In the absence of any other criteria, the thickness of the Ta converter foil is usually chosen to maximize the forward going X-ray energy, the extraction efficiency. For pulsed machines, this optimization can only be done theoretically using data like that of Fig. 7, since this quantity cannot be measured directly. In fact, it is more appropriate to maximize the response, or some stress parameter,[30] of a particular experiment. This can be especially important for low-energy simulators because of the strong energy dependence of the photon interaction cross sections in the photoelectric region. An example of this situation is illustrated in Fig. 18 where we compare the extraction efficiency with the mean deposition over 573 cm^2 as a function of the thickness of the Ta foil at 1.0 and 2.0 MeV. The maxima for energy deposition and extraction efficiency do not occur at the same thickness. Furthermore, the slopes on either side of the maxima behave differently; the extraction efficiencies increase more rapidly on the up side, and the depositions decrease more rapidly on the down side. Thus, the penalty to be paid for missing the maxima are different. Each measured or calculated response will have its own unique dependence (in particular, its own unique maximum) on converter thickness.

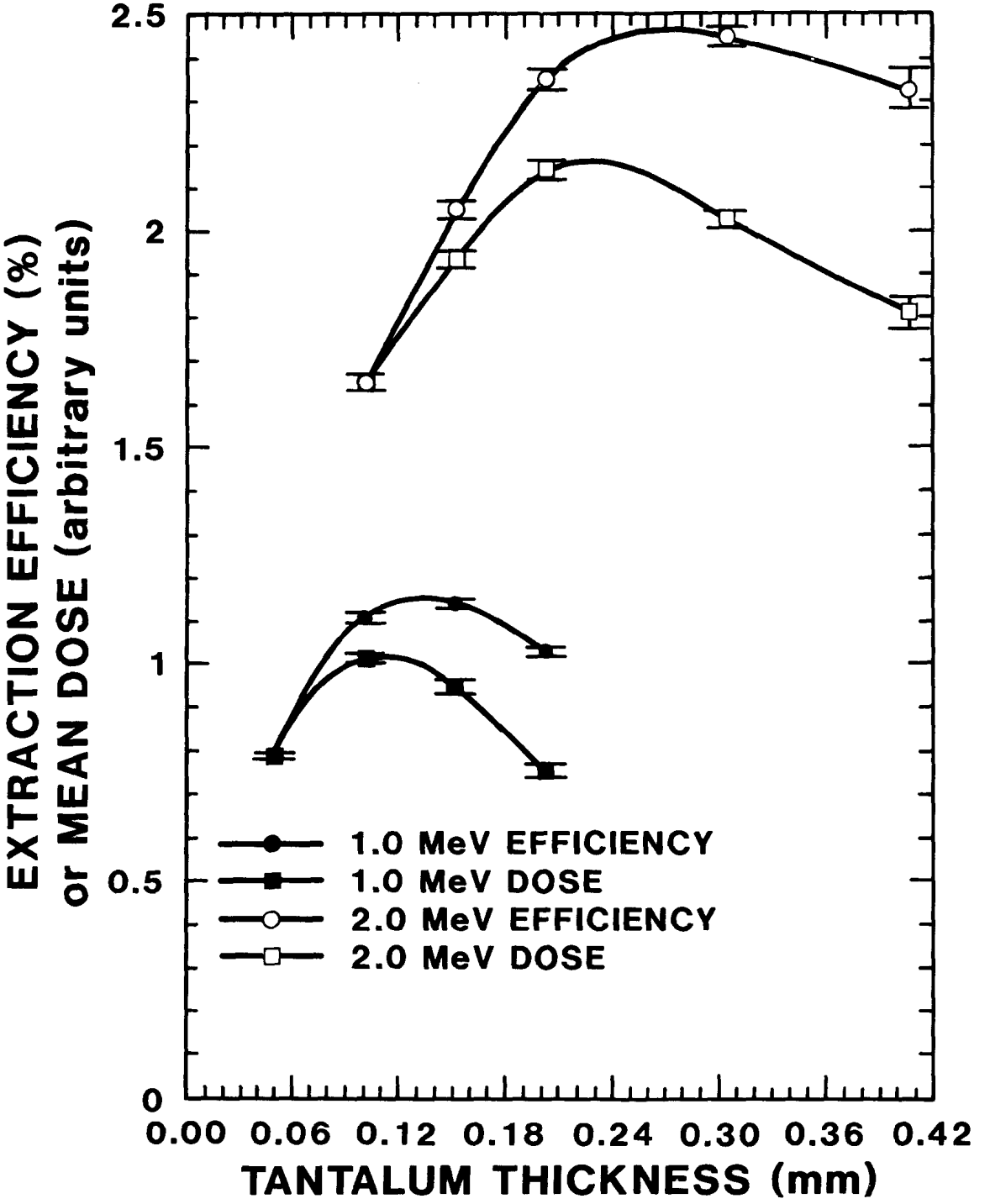

Fig. 18. Extraction efficiency in the forward 2π solid angle and mean energy deposition over an area of 573 cm^2 in CaF_2 (TLD) as a function of the thickness of the tantalum converter foil calculated via the NE method at source electron kinetic energies of 1.0 and 2.0 MeV.

5.1.2 The FT Method --- Reference 27 shows that of the four conditions stated in the appendix that are responsible for the breakdown of the NE method (see appendix) it is condition (b) that is responsible for the underprediction of the TLD deposition. That is, it is energy deposition from the buildup of incoherently scattered photons within the TLD configuration itself that is not accounted for. In this subsection, we compare the calculated TLD deposition obtained from the FT method for the 4.0-cm axial plane with the predictions of the NE method. The scheme employed for carrying out the FT calculations is outlined in the appendix.

The radial profiles for a source electron energy of 2.0 MeV and a 0.20-mm-thick Ta converter are compared in Fig 19. The mean energy depositions over the 573-cm^2 area at this same converter thickness are compared in Fig. 20 as a function of source electron energy. And finally, in Fig. 21, the mean depositions for a source energy of 1.0 MeV are compared as a function of the thickness of the converter foil. All three comparisons show the systematic underprediction of the NE method. In Fig. 19, the estimated one-sigma statistical uncertainties for the FT method are not quite as good as those of the NE method (see discussion of Fig. 16), ranging from 2% in the highest radial bin to 10% in the lowest.

The data in Figs. 19-21 seem at first to be evidence against the usefulness of the NE method for prediction the TLD deposition. However, just the opposite is true. These data show that there is only a slight dependence of the underprediction of the NE method on source electron energy, converter thickness, and photon angle of incidence at the detector (i. e., radial profile). It is so small as to be almost masked by the

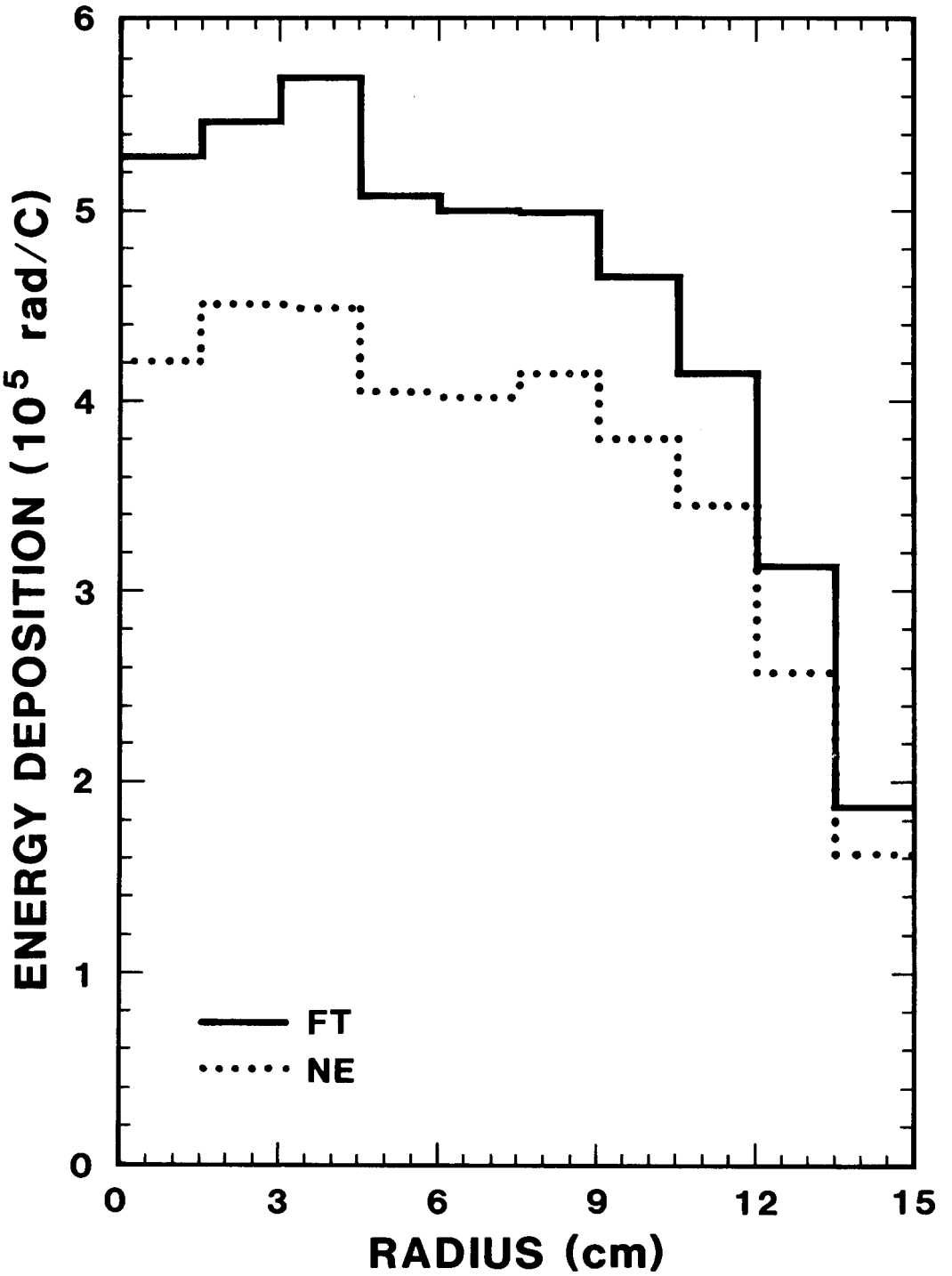

Fig. 19. Comparison of radial energy deposition profiles in CaF_2 (TLD) at an axial distance of 4.0 cm from the upstream surface of the converter foil calculated via the FT and NE methods for a source electron kinetic energy of 2.0 MeV and a 0.20-mm-thick tantalum converter foil.

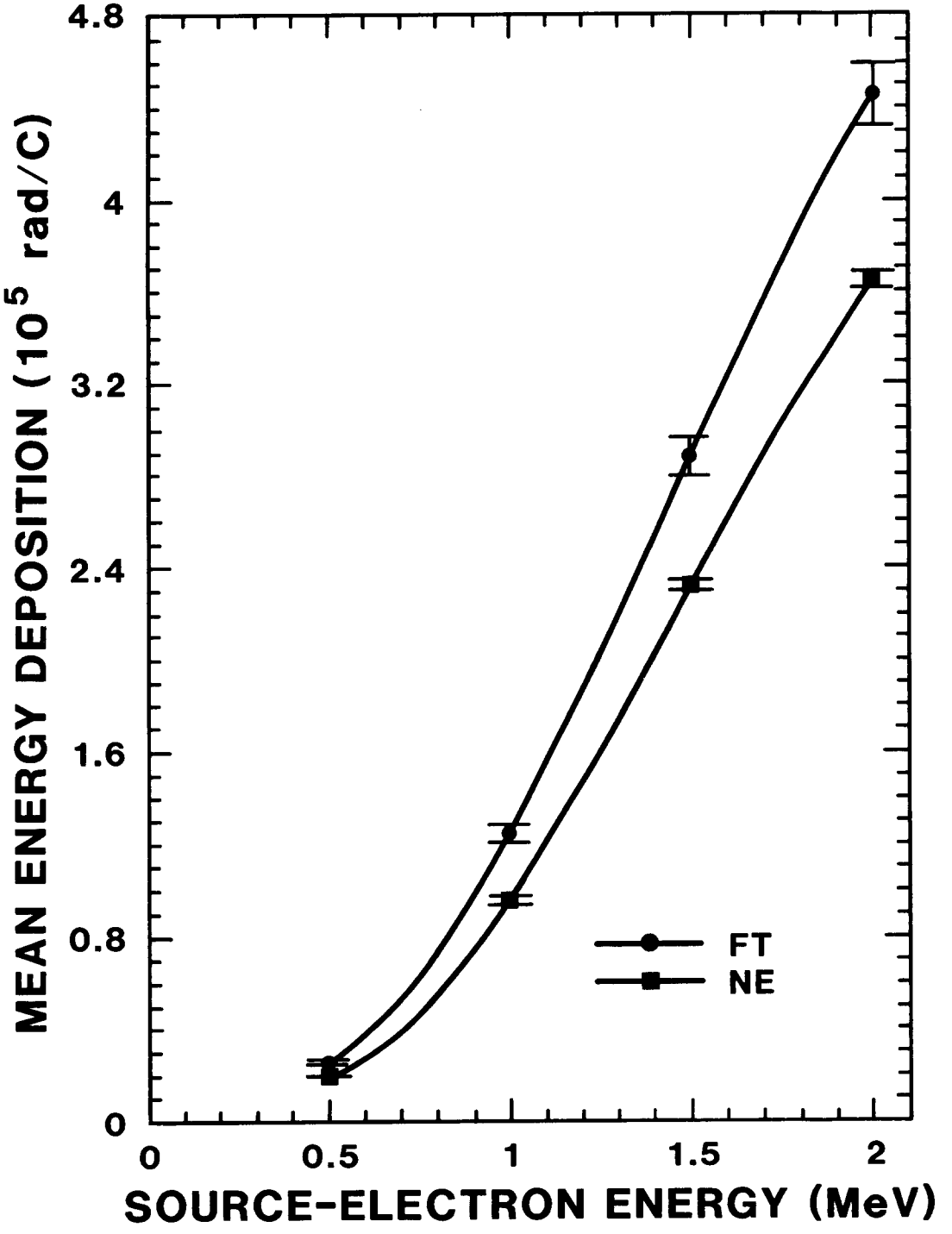

Fig. 20. Comparison of mean energy deposition over an area of 573 cm^2 in CaF_2 (TLD) at an axial distance of 4.0 cm from the upstream surface of the converter foil as a function of the source electron kinetic energy calculated via the FT and NE methods with a 0.20-mm-thick tantalum converter foil.

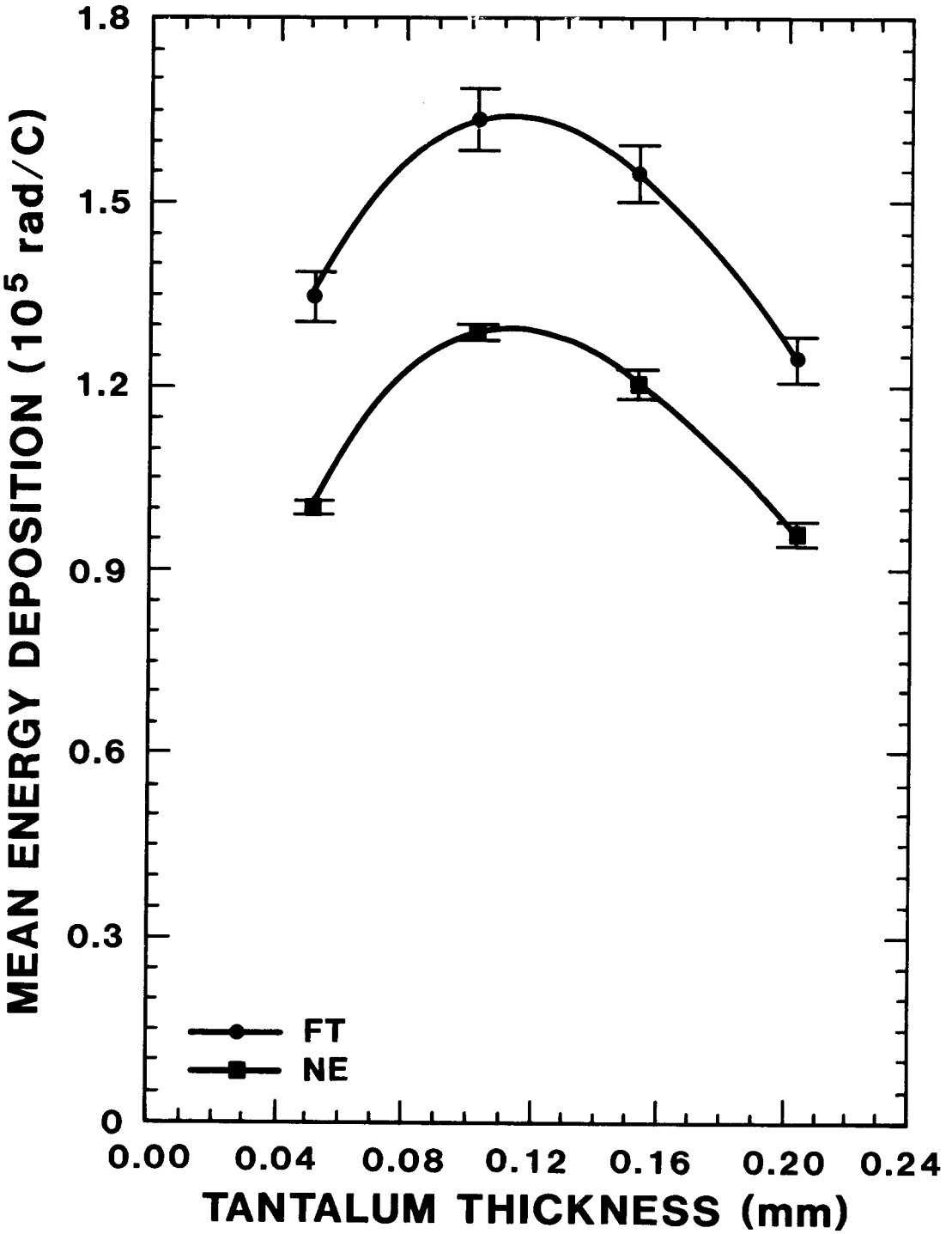

Fig. 21. Comparison of mean energy deposition over an area of 573 cm^2 in CaF_2 (TLD) at an axial distance of 4.0 cm from the upstream surface of the converter foil as a function of the thickness of the tantalum converter foil calculated via the FT and NE methods for a source electron kinetic energy of 1.0 MeV.

approximate 1% statistical uncertainties of the average deposition over the axial plane and the approximate 1-6% statistical uncertainties of the radial profiles (larger uncertainties at small radii corresponding to smaller solid angles). The average ratio of the mean deposition over the 573-cm^2 area obtained from the NE method to that obtained from the FT method for all of the cases shown in Figs. 20-21 is 0.78 ± 0.03. Consequently, to a very good approximation, all NE results, differential or integral, can be scaled by this ratio. Thus, further predictions by the more costly FT method of dosimetry measured with these particular TLDs for the baseline Saturn diode become unnecessary. Furthermore, a similar scaling for CaF_2 TLDs with a much thinner Al equilibration should be even more accurate because the reduced Compton buildup will result in a much smaller correction between the NE and FT predictions, as is shown in Ref. 27.

5.2 Si Dose

Of course, the specifications for Saturn are given in terms of dose to silicon. Such specifications must inevitably be somewhat illusory since the energy deposition in the Si portions of actual test devices is never directly measured. This situation is further exacerbated by the fact that the Si in actual devices is rarely, if ever, in electron equilibrium. Thus, the dose to Si becomes a function of its local environment. This means that, even for a given radiation output and a given location for the subsystems to be tested, different Si elements within the same subsystem and the same Si element within different subsystems may receive different depositions of both charge and energy. These caveats should be respected in

any discussion of X-ray deposition in Si. In what follows, we employ the FT method to investigate (a) the dose to Si in an environment equivalent to that of the CaF_2 in Sec. 5.1 and (b) the free-field energy deposition profile in Si.

5.2.1 Relative to TLD Dose --- One reason for the popularity of CaF_2 is the presumed similarity with Si of its response to β and γ radiation. Whether or not this similarity extends to X-ray environments is much less certain because of the strong atomic number dependence of photoelectric cross sections. Here, we provide information necessary for converting measured TLD dose to an equivalent dose in Si.

The equivalent Si deposition is obtained by replacing the CaF_2 in the TLD configurations by an equivalent areal density of Si. Using 3.18 and 2.33 g/cm^3 for the densities of CaF_2 and Si, respectively, we replace the 0.89 mm of the former by 1.21 mm of the latter. The upstream face remains fixed at the 4.0-cm axial plane.

The radial profiles calculated with the FT method for both Si and TLDs are compared for the four source electron energies in Figs. 22 through 25. The converter thickness is 0.20 mm in all cases. Also shown are the TLD profiles obtained using the NE method. The estimated one-sigma statistical uncertainties of the Si results are usually less than or equal to 5%, except for the lowest radial bin where they are about 10% (see discussion of Fig. 19 for uncertainties in TLD results). The ratio of the mean deposition in Si to that in CaF_2 over 573 cm^2 is plotted in Fig. 26 as a function of

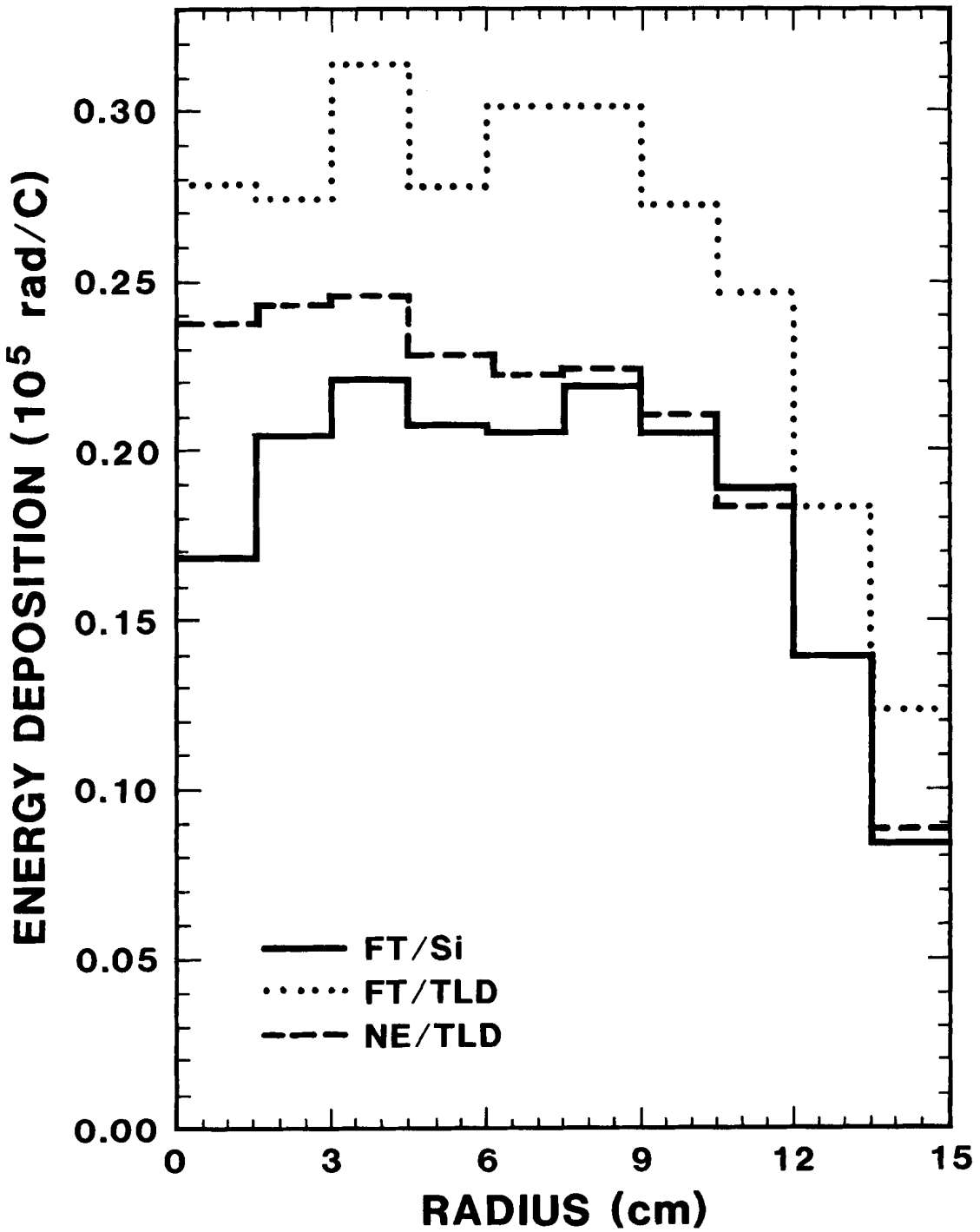

Fig. 22. Comparison of radial energy deposition profiles in CaF_2 (TLD) and equivalent Si at an axial distance of 4.0 cm from the upstream surface of the converter foil calculated via the FT method for a source electron kinetic energy of 0.5 MeV and a 0.20-mm-thick tantalum converter foil. Also shown is the TLD profile calculated via the NE method.

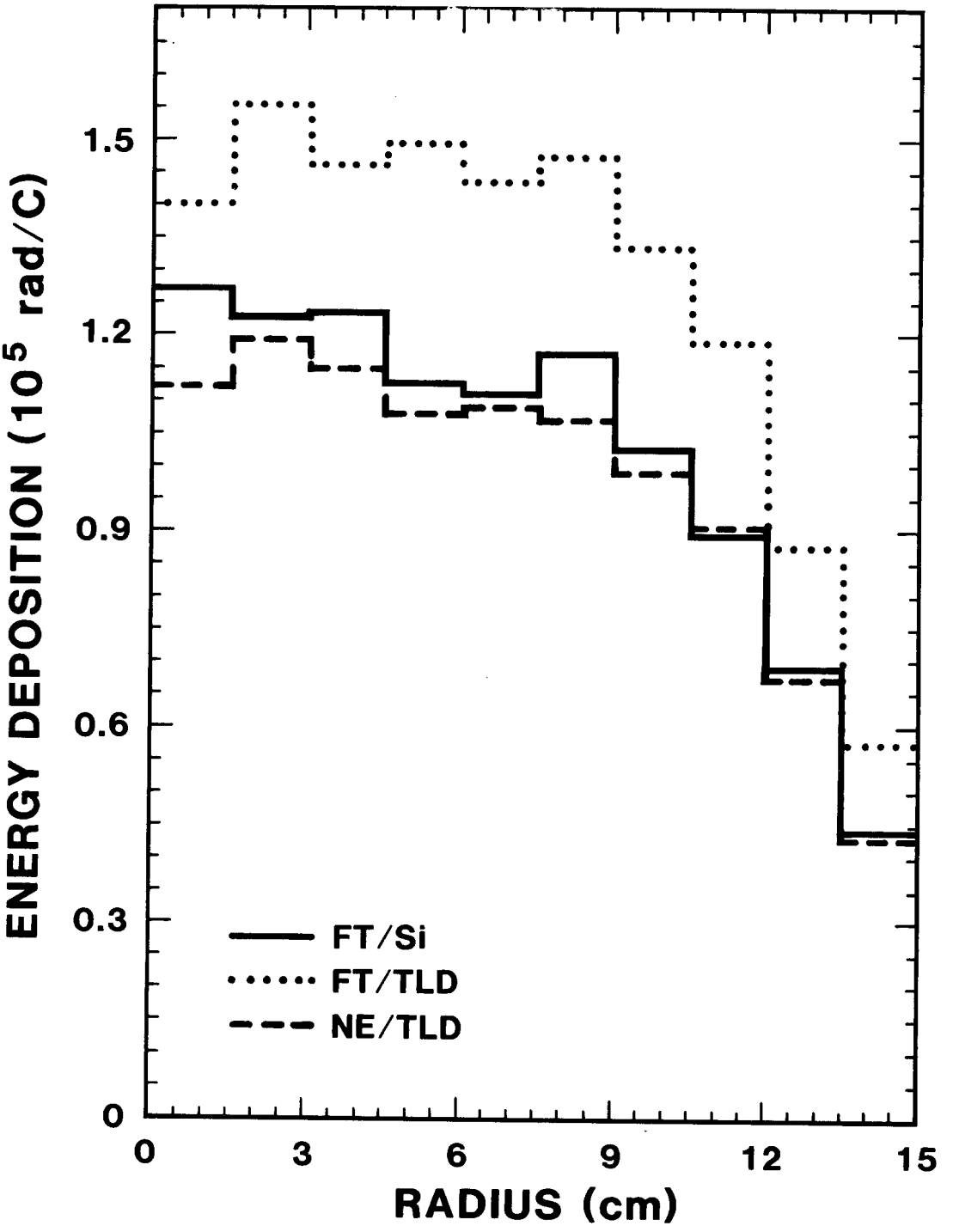

Fig. 23. Comparison of radial energy deposition profiles in CaF_2 (TLD) and equivalent Si at an axial distance of 4.0 cm from the upstream surface of the converter foil calculated via the FT method for a source electron kinetic energy of 1.0 MeV and a 0.20-mm-thick tantalum converter foil. Also shown is the TLD profile calculated via the NE method.

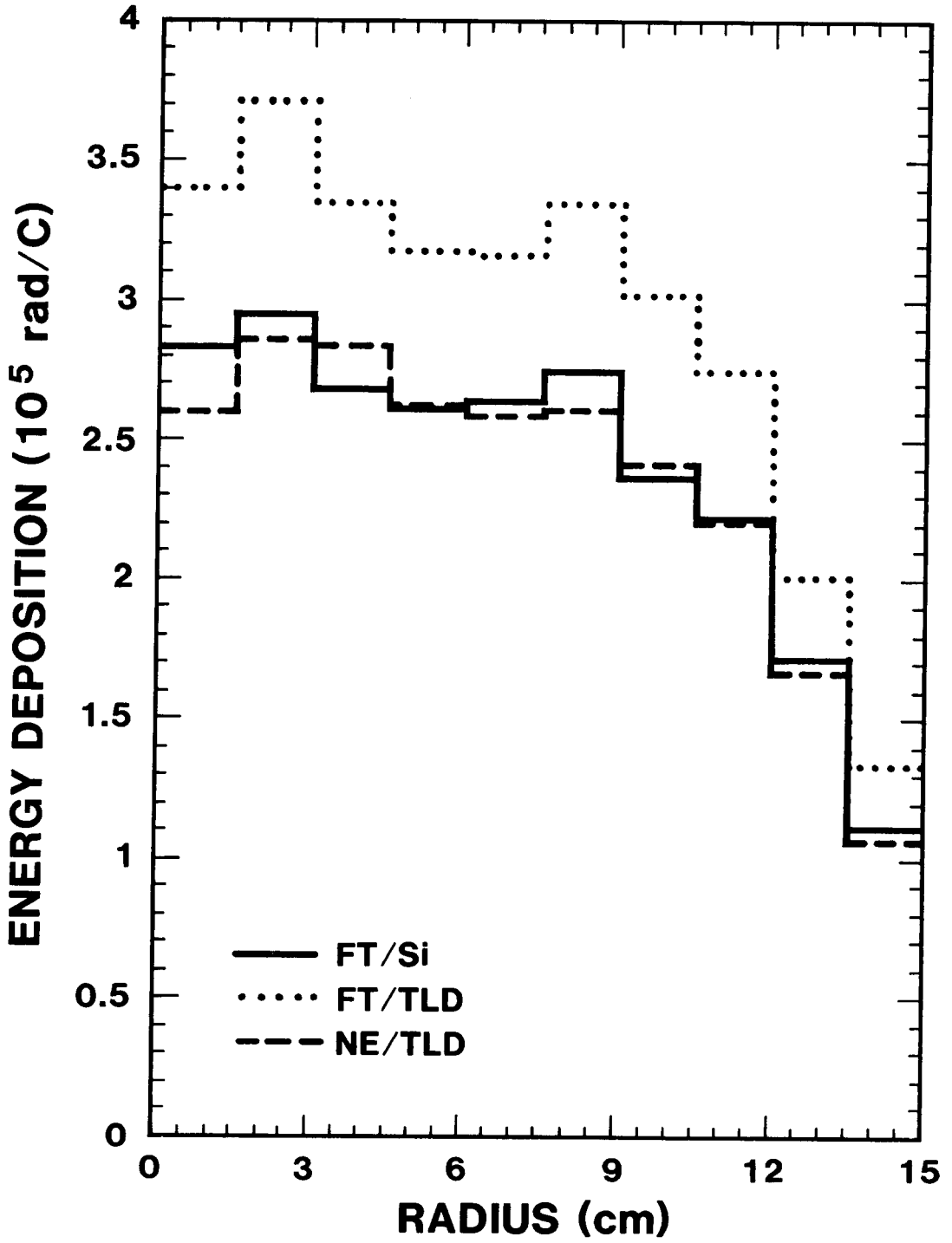

Fig. 24. Comparison of radial energy deposition profiles in CaF_2 (TLD) and equivalent Si at an axial distance of 4.0 cm from the upstream surface of the converter foil calculated via the FT method for a source electron kinetic energy of 1.5 MeV and a 0.20-mm-thick tantalum converter foil. Also shown is the TLD profile calculated via the NE method.

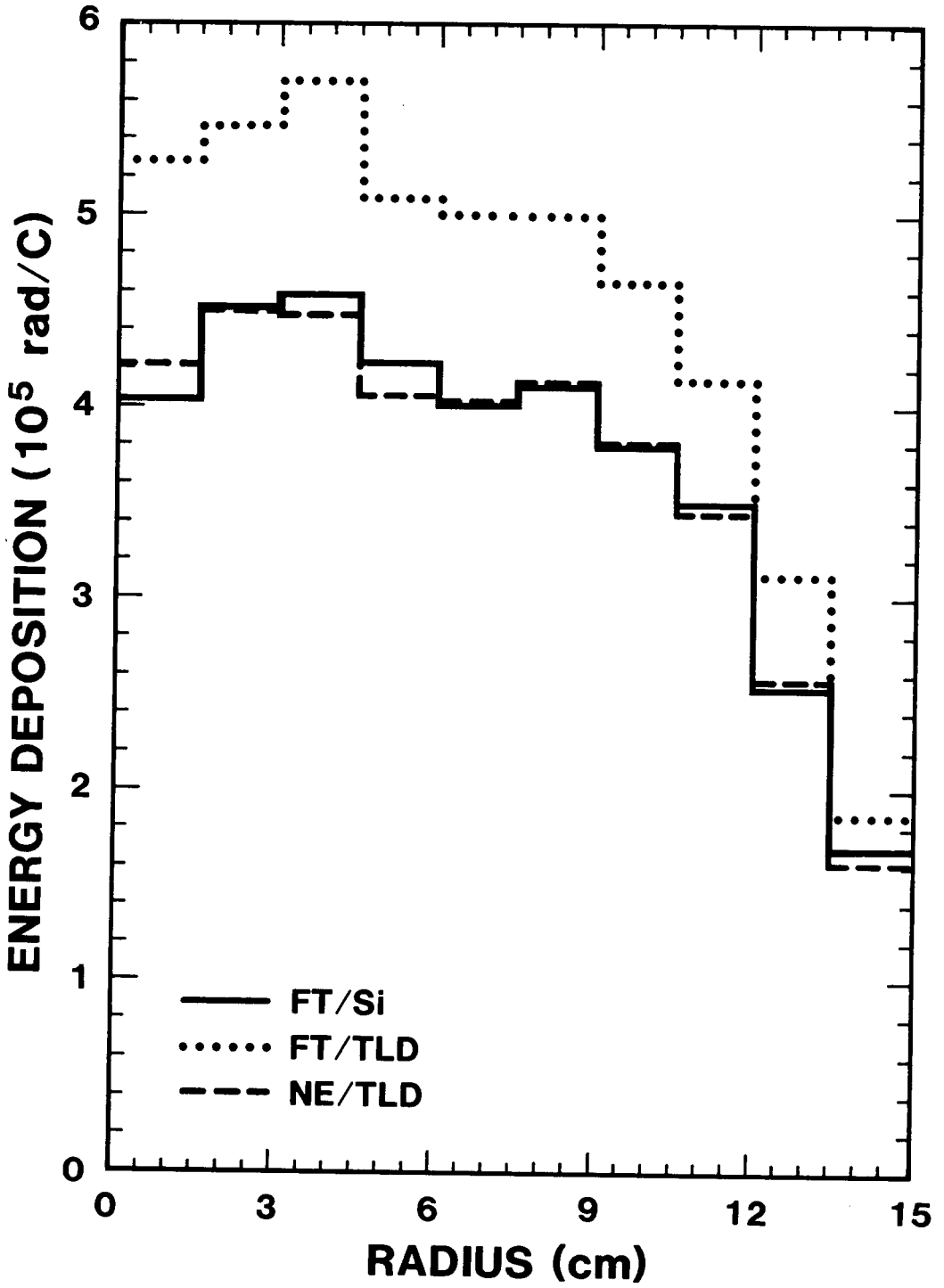

Fig. 25. Comparison of radial energy deposition profiles in CaF_2 (TLD) and equivalent Si at an axial distance of 4.0 cm from the upstream surface of the converter foil calculated via the FT method for a source electron kinetic energy of 2.0 MeV and a 0.20-mm-thick tantalum converter foil. Also shown is the TLD profile calculated via the NE method.

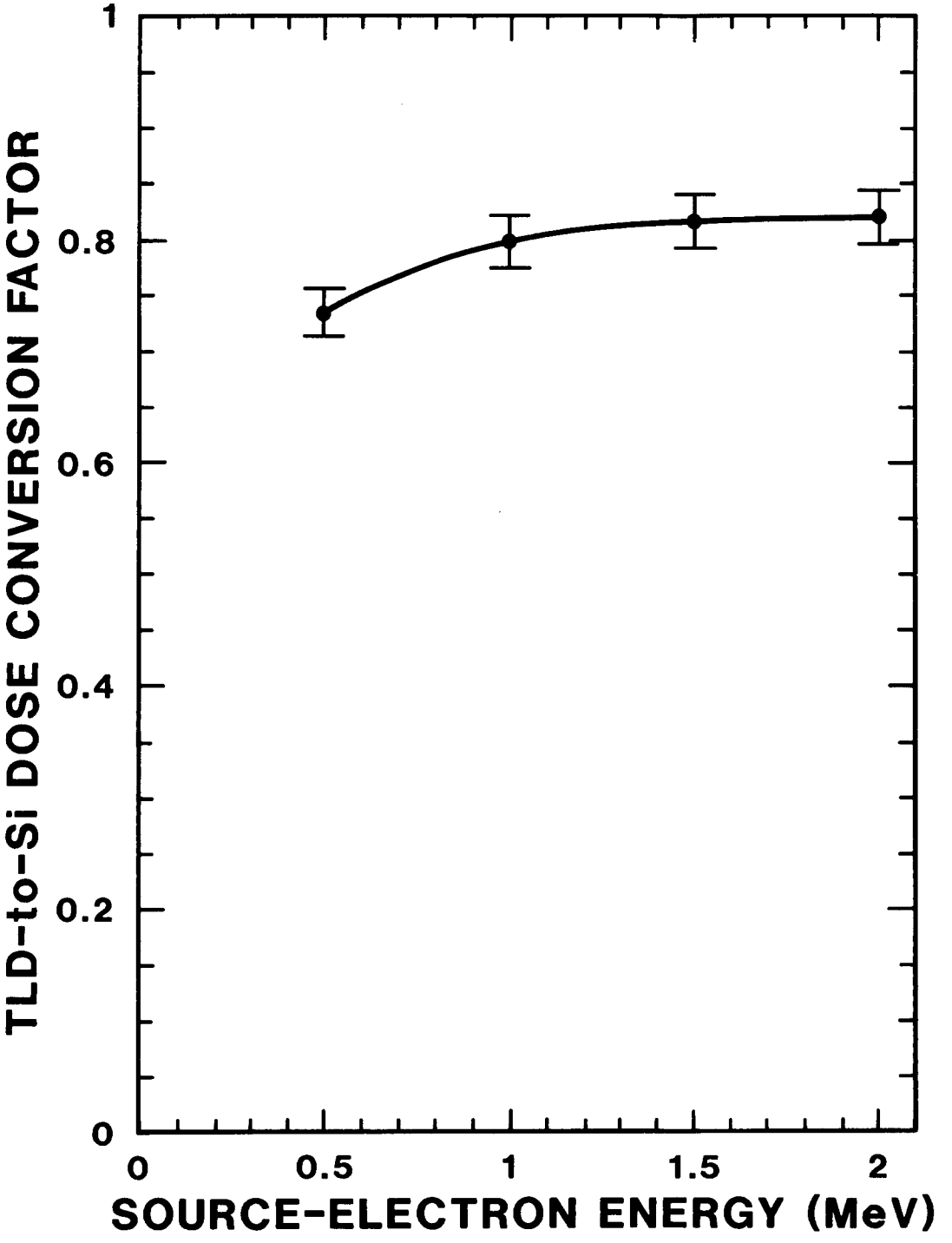

Fig. 26. TLD-to-equivalent-Si conversion factor as a function of the source electron kinetic energy calculated via the FT method.

electron energy. The increase in this ratio with source electron energy is presumably due to a decrease in the importance of photoelectric interaction and the attendant decrease in importance of the Ca constituent of the TLD. The data in Fig. 26 can be used to convert measured or predicted TLD deposition to bulk Si deposition.

Coincidentally, Figs. 22-26 show that the factors needed to convert the measured TLD deposition to bulk Si dose in the same environment are very nearly the inverse of the correction factors that must be applied to predictions of TLD deposition that have been obtained in the NE approximation.

5.2.2 Free-Field Energy Deposition --- On the one hand, since we know that the Al equilibration of the previous subsection is excessive, it is of interest to study the dose that can be achieved in Si with a minimum of equilibration. On the other, it is of interest to know what constitutes minimum equilibration or, equivalently, to know the equilibration depth for different source electron energies.

We obtain this information by calculating high-resolution axial energy deposition profiles in Si. We use the FT method because we are specifically interested in investigating the question of electron equilibrium. We replace the X-ray target configuration of the previous subsection with a free standing 15.0-cm-radius disk of Si. The disk is subdivided into an appropriate number of axial layers so that the resulting energy depositions

are averaged over the full area of the disks. Again, the upstream surface of the disk is fixed at the 4.0-cm standoff distance.

The axial profiles are shown in Figs. 27 through 30 for disk thicknesses of 50, 100, 150, and 250 μm at source electron energies of 0.5, 1.0, 1.5, and 2.0 MeV, respectively. Estimated one-sigma statistical uncertainties are almost always 5% or better. The region near the upstream surface is more nearly equilibrated than that of the downstream surface. This occurs primarily because in these close-in geometries some equilibration of the upstream surface is provided by the converter itself.[31] The reduced equilibration at the upstream surface for low source energies supports this explanation, because the broader angular distributions of the particles escaping the Kevlar at lower source energies means that more of these particles will miss the Si disk.

Based on the results of Figs. 27-30, we postulate conservatively large equilibration depths of 25, 50, 75, and 125 μm for Si at source electron energies of 0.5, 1.0, 1.5, 2.0 MeV, respectively. Since the thicknesses of Si elements of electronic components and subsystems typically range from a fraction of 1 μm to a few tens of microns, the response of such devices to any X-ray environment will always be of an intrinsically nonequilibrium nature.

We can also use these profile data to study the penalty paid for excessive equilibration in the previous subsection. The mean depositions in the TLD-equivalent Si of Figs. 22-25, averaged over the full 15.0-radius, are 0.17, 0.89, 2.1, and 3.3 rad/C at source energies of 0.5, 1.0, 1.5, and

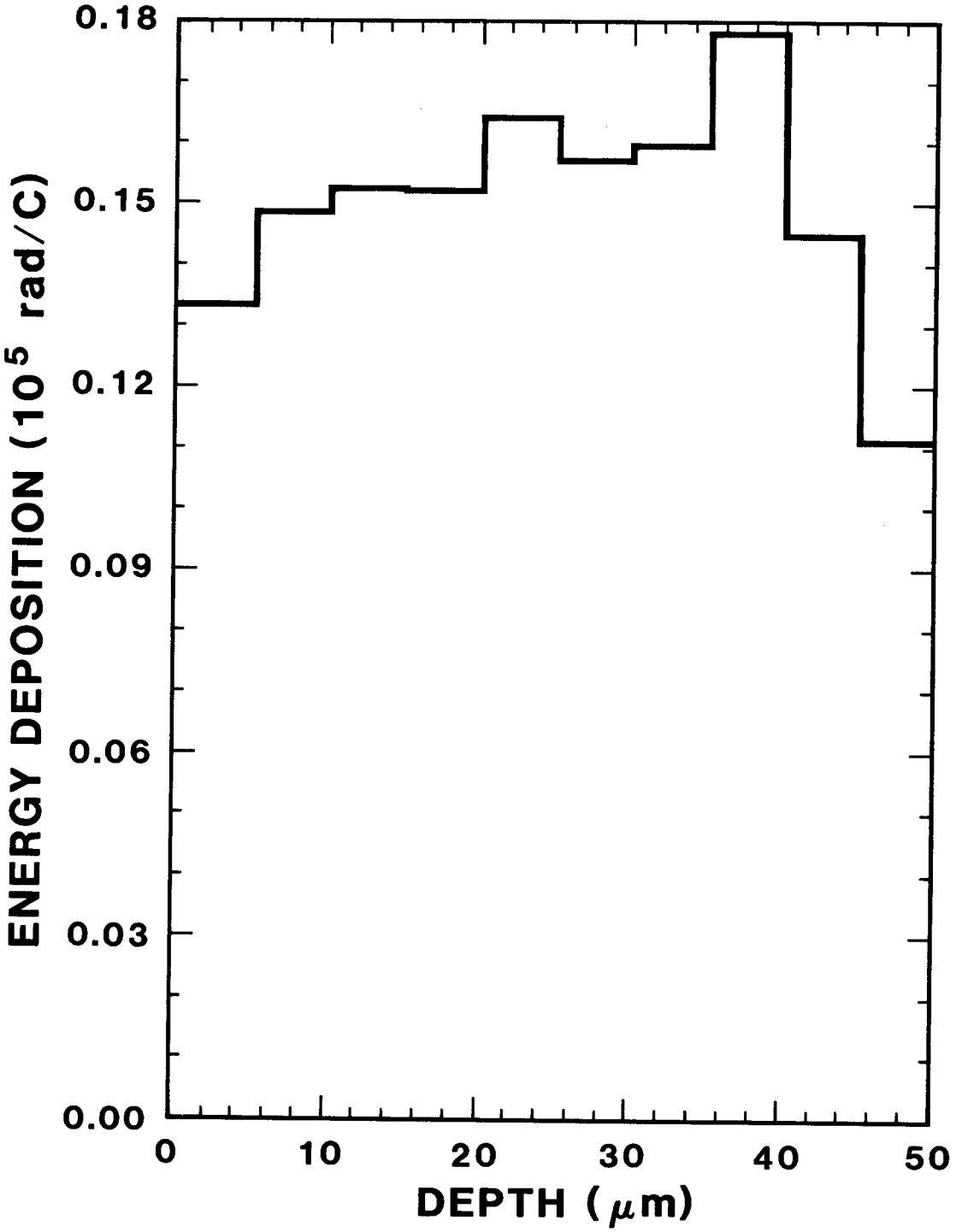

Fig. 27. Axial energy deposition profile through a 50-μm-thick disk of Si averaged over the full 15.0-cm-radius area, and calculated via the FT method for a source electron kinetic energy of 0.5 MeV and a 0.20-mm-thick tantalum converter foil -- the front surface of the disk is 4.0 cm from the upstream surface of the converter foil.

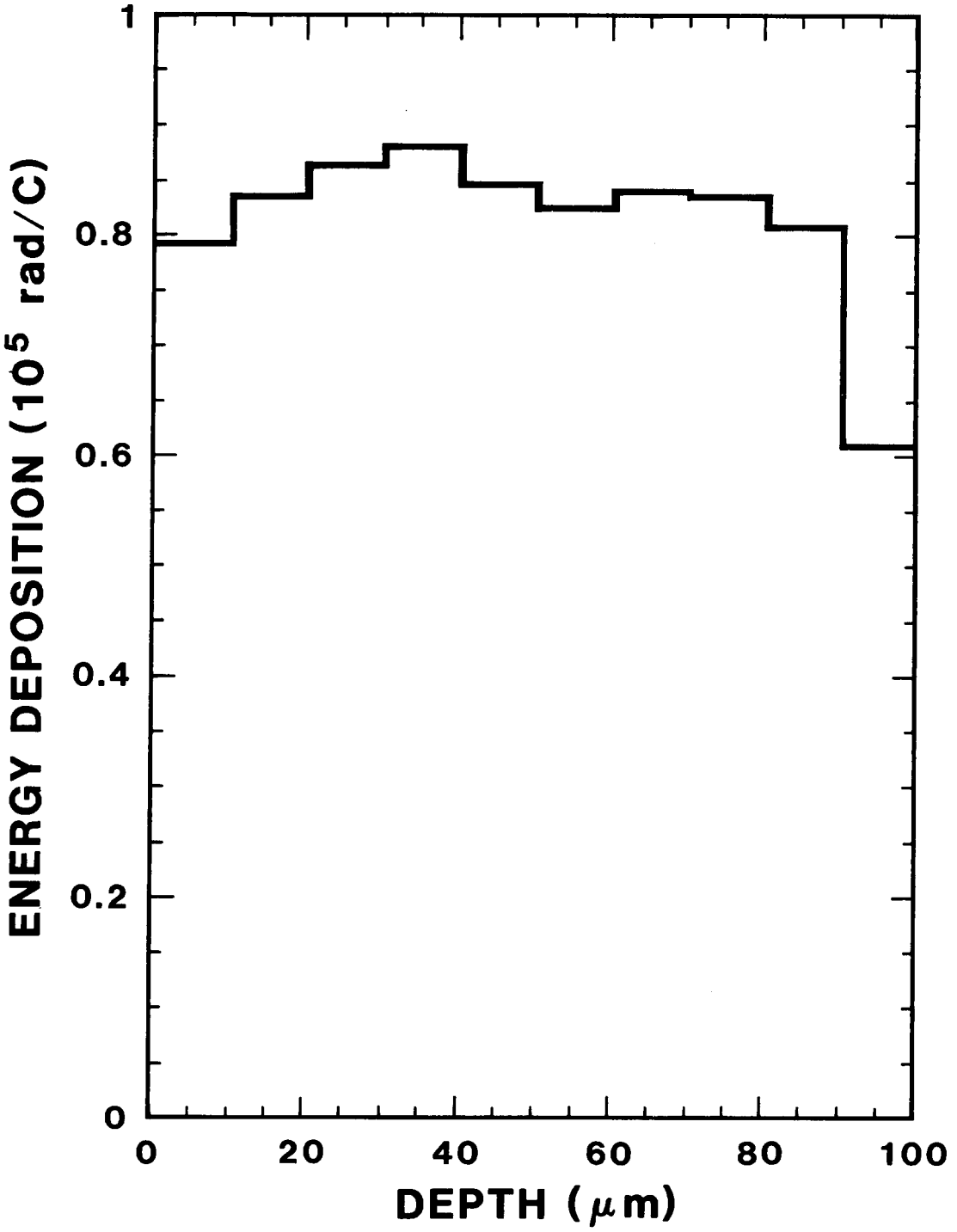

Fig. 28. Axial energy deposition profile through a 100-μm-thick disk of Si averaged over the full 15.0-cm-radius area, and calculated via the FT method for a source electron kinetic energy of 1.0 MeV and a 0.20-mm-thick tantalum converter foil -- the front surface of the disk is 4.0 cm from the upstream surface of the converter foil.

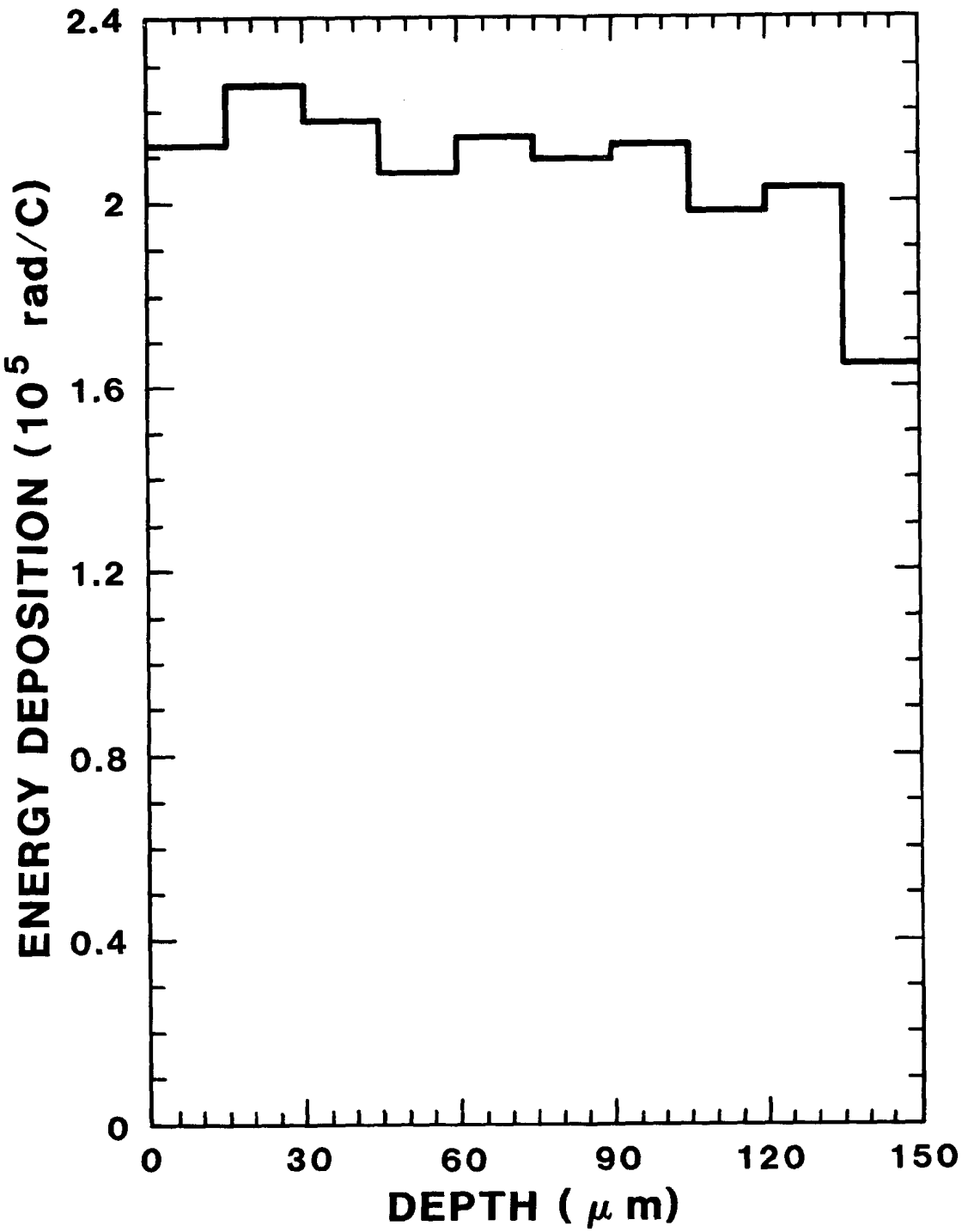

Fig. 29. Axial energy deposition profile through a 150-μm-thick disk of Si averaged over the full 15.0-cm-radius area, and calculated via the FT method for a source electron kinetic energy of 1.5 MeV and a 0.20-mm-thick tantalum converter foil -- the front surface of the disk is 4.0 cm from the upstream surface of the converter foil.

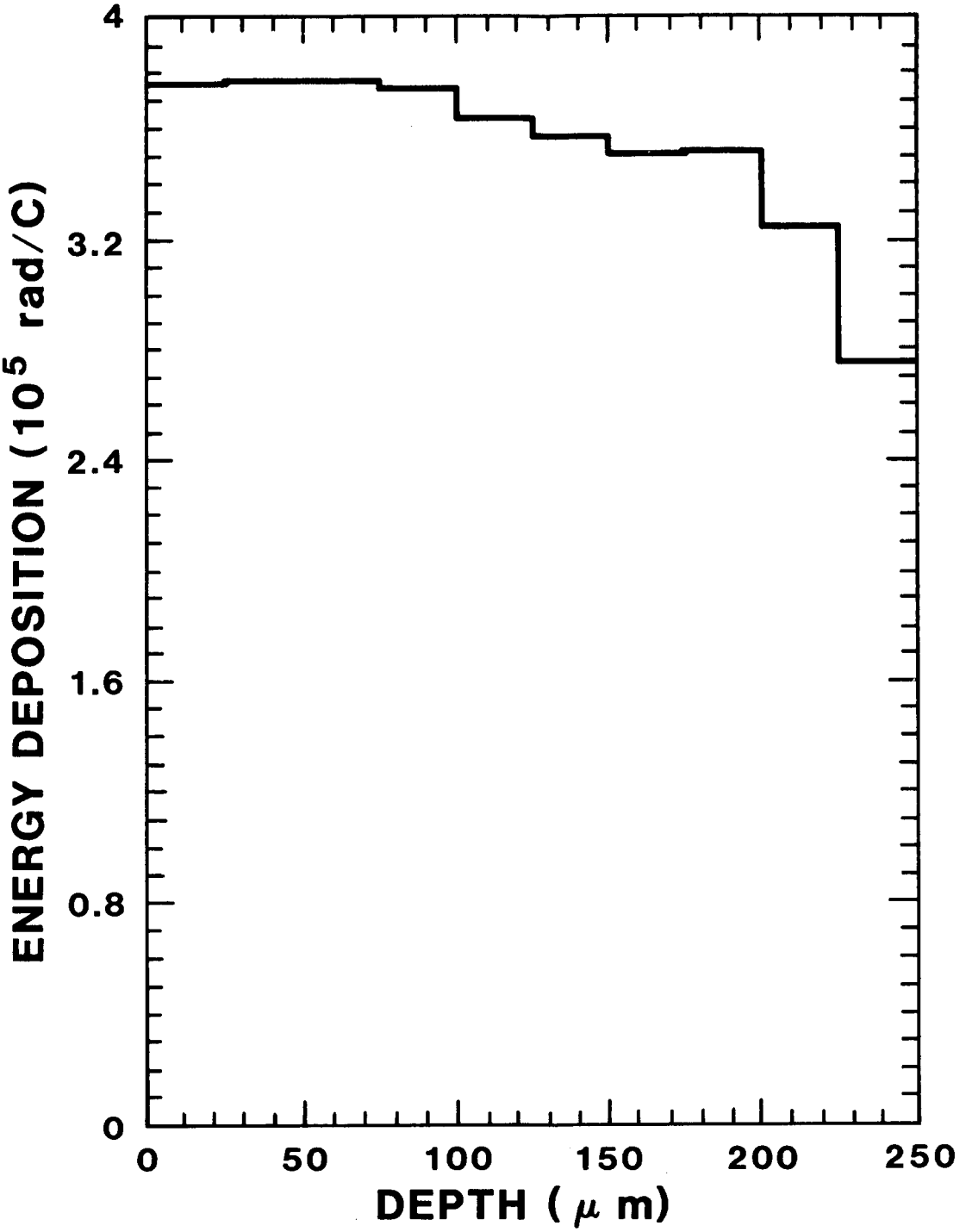

Fig. 30. Axial energy deposition profile through a 250-μm-thick disk of Si averaged over the full 15.0-cm-radius area, and calculated via the FT method for a source electron kinetic energy of 2.0 MeV and a 0.20-mm-thick tantalum converter foil -- the front surface of the disk is 4.0 cm from the upstream surface of the converter foil.

2.0 MeV, respectively, with statistical uncertainties of less than 5%. These are in relatively good agreement with the equilibrium doses in Figs. 27-30. We conclude that the penalty for the excessive equilibration used in the standard TLD packaging employed exclusively in this report is negligible, and we may continue to take advantage of the convenience of this packaging in routine dosimetry. From our comparison of the FT and NE predictions of the TLD deposition, it appears that the buildup of incoherently scattered radiation in the Al encapsulation compensates for the attenuation in that encapsulation. This conclusion is consistent with the experimental and theoretical results in Fig. 16 of Ref. 17 and Ref. 29 employing this same encapsulation, which show little reduction in TLD dosimetry of the X rays from monoenergetic 0.75-MeV electrons using an optimized Ta converter. However, those same references show a substantial penalty for that dosimetry in the softer X-ray environment obtained from a graphite converter. In fact, one could probably get by with no TLD equilibration at all in the Saturn environment; since the thickness of the CaF_2 is much greater than our conservative equilibration thicknesses, the effect of the lack of equilibration would be difficult to detect.[17,29]

6. Primary Electron Deposition in the Converter Configuration

Although primary deposition in the converter configuration high enough for both anode plasma formation and severe thermomechanical damage is a foregone conclusion, predictions of the deposition would facilitate quantitative analysis of these phenomena. Moreover, these predictions would provide some preliminary information in anticipation of the inevitable

application of Saturn in the direct-electron or extracted-beam mode for the systematic study of these and other phenomena such as high-temperature, high-pressure equation-of-state research.

In addition to all the other information obtained from the NE method, we also obtain two-dimensional estimates of the source electron deposition in the converter configuration. Unfortunately, the three-ring source is so nonuniform that these estimates do not provide sufficient resolution of the deposition profiles. Moreover, in eventual direct-electron experiments, the electron distribution could well be quite different from the one considered here.

Until more detailed calculations are carried out for precise experimental geometries, deposition can best be estimated by normalizing one-dimensional deposition data to expected current densities. A comprehensive database for energies up to 1.0 MeV is available in Ref. 32. Since stopping powers are only weakly dependent on electron energy, the 1.0-MeV data can be used with reasonable accuracy up to 2.0 MeV if depths are expressed in units of the electron CSDA (continuous-slowing-down-approximation) range.[33] Suppose, for example, we wanted to estimate the saturated surface deposition (in principle, a semi-infinite thickness; in practice, less than a CSDA range) in graphite and Ta anodes at the middle ring of our three-ring source. A conservative estimate of the graphite and Ta surface depositions for the energy range 0.5-2.0 MeV is 1.5 and 2.0 $(MJ/g)/(C/cm^2)$, respectively. Assuming 1/3 of a total of 0.25 C/pulse to be distributed uniformly over an annulus from 7.5 to 8.5 cm, the estimated surface deposition in graphite and Ta is 2.5 and 3.3 kJ/g, respectively.

7. Conclusions

The general conclusion of this work is that the Saturn baseline diode, if operated at 2.0 MeV with a peak current of 12.5 MA and a pulse width of 20 ns, will meet the project design criteria for dose, dose rate, and radial uniformity.

In addition, this analysis has resulted in a number of secondary findings that may be of interest to those responsible for operation of the facility, those involved in further source development, and potential users:

a) Under nominal conditions, about 2% of the beam energy, or 10 kJ, should be available for the simulation of X-ray effects.

b) A 0.20-mm Ta converter foil, in conjunction with the converter configuration described in Sec. 3, will maximize the extraction efficiency for a source electron kinetic energy somewhere between 1.0 and 2.0 MeV.

c) Taking advantage of the design flexibility for operating the facility at reduced voltages in order to obtain a softer X-ray spectrum will result in a penalty in output efficiency as given by Fig. 3.

d) Two-dimensional effects that may be sensitive to details of the experimental converter configuration will result in a complex X-ray field (strong spatial/angular/energy coupling) for close-in exposures.

e) In none of the axial exposure planes from 2.5 to 10.0 cm downstream of the converter foil will the dose vary by more than a factor of two over a 500-cm^2 area. The reduction in the mean deposition as the location of the exposure plane is increased from 2.5 to 10.0 cm will be less than a factor of two.

f) For a 20-ns pulse at an effective energy of 2.0 MeV and with a peak current of 12.5 MA, the NE method predicts lower bounds for the peak dose and dose rate in the standard TLDs of about 1.4×10^5 rad and 6.8×10^{12} rad/s, respectively, at an axial distance of 2.5 cm. When corrected with the factor by which the NE method is known to underpredict the deposition in this energy range, these values increase to 1.7×10^5 rad and 8.7×10^{12} rad/s, respectively.

g) As a function of the thickness of the Ta converter foil, the maxima for energy deposition and extraction efficiency do not occur at the same thickness. In principle, each particular radiation response will have its own unique dependence on converter thickness. This response could be maximized experimentally or with the aid of code predictions.

h) To a very good approximation within the parameter space covered by this report, all NE predictions of energy deposition can be corrected by a single constant scale factor which is independent of radial location, source electron kinetic energy, and thickness of the Ta converter foil. Thus, predictions by the more costly FT method become unnecessary.

i) The factor (about 0.8) needed to convert measured or predicted TLD deposition to bulk Si deposition in an equivalent environment is only weakly dependent on source electron kinetic energy (Fig. 26) for the 0.20-mm Ta converter foil.

j) The region near the upstream surface of a freestanding Si X-ray target is more nearly equilibrated than that of the downstream surface. This occurs primarily because in these close-in geometries some equilibration of the upstream surface is provided by the converter itself.

k) Conservatively large equilibration depths are postulated at 25, 50, 75, and 125 μm for Si at source electron energies of 0.5, 1.0, 1.5, 2.0 MeV, respectively. Consequently, the response of Si elements of electronic components and subsystems to the Saturn or a postulated threat X-ray environment will always be of an intrinsically nonequilibrium nature.

l) The penalty in reduced deposition for the excessive equilibration in the standard TLD packaging used exclusively in this report is negligible when high-Z converter foils such as Ta are employed.

m) For Saturn pulses of 0.25 C at current densities typical of the baseline diode, direct-electron surface depositions in excess of 1 kJ/g are possible in all materials.

Finally, there are three major caveats and/or warnings concerning this work:

1) The electron albedo from the Ta converter foil is significant (Fig. 6). A portion of the radiation that would otherwise have been produced by these electrons may be recovered through reinjection by the electric field of the diode. This potential increase in the radiation production has not been accounted for in this report.

2) The bremsstrahlung cross sections currently being used in the ITS system are not the best available. They are based on the Born approximation, and the range of electron energies and converter materials for which they are least accurate closely correspond to those of this report.

3) Bulk TLD or bulk Si dose and dose rates are merely standards for cross calibrating or characterizing X-ray sources of approximately the same spectra and may deviate significantly from the doses and dose rates in the unequilibrated Si elements of components or subsystems exposed to these sources.

References

1. K. R. Prestwich, J. R. Lee, J. J. Ramirez, T. W. L. Sanford, F. J. Agee, G. R. Frazier, and A. R. Miller, Proceedings of the 1987 Particle Accelerator Conference, March 16-19, 1987, Washington, D. C., to be published.

2. J. E. Powell and J. A. Reuscher, Proceedings of the US/UK JOWOG-6 Meeting, June 14-17, 1983, Albuquerque, NM, (U) SAND83-2239, RS3151/84/013, Sandia National Laboratories, June 1984, p. 7 (classified).

3. D. D. Bloomquist, R. W. Stinnett, D. H. McDaniel, J. R. Lee, A. W. Sharpe, J. A. Halbleib, L. G. Schlitt, P. W. Spence, and P. Corcoran, Proceedings of the 6th IEEE Pulsed Power Conference, June 29-July 1, 1987, Arlington, VA, to be published.

4. J. D. Boyes, J. S. Cap, G. M. Douglas, T. L. Franklin, J. M. Hart, H. C. Ives, S. J. Robischon, B. L. Smith, W. O. Stoppkotte, D. M. VanDeValde, E. A. Weinbrecht, T. L. Woolston, R. G. Altes, and D. L. Pellow, Proceedings of the 6th IEEE Pulsed Power Conference, June 29-July 1, 1987, Arlington, VA, to be published.

5. T. H. Martin, J. P. VanDevender, G. W. Barr, S. A. Goldstein, R. A. White, and J. F. Seamen, IEEE Trans. Nucl. Sci., NS-28, No. 3, 3368 (1981).

6. C. R. McClenahan, T. P. Wright, J. P. Quintenz, R. C. Backstrom, and P. W. Spence, "Triaxial Diode on Hydramite," SAND85-0740, Sandia National Laboratories, October 1985.

7. M. A. Hedemann, A. L. Pregenzer, J. R. Lee, R. J. Leeper, J. S. Gustwiller, P. W. Spence, and H. Kishi, Proceedings of the 6th IEEE Pulsed Power Conference, June 29-July 1, 1987, Arlington, VA, to be published.

8. E. D. Reedy, Jr., M.A. Hedemann, and M. A. Stark, "Hydramite II Screening Test of Potential Bremsstrahlung Converter Debris Shield Materials," SAND86-0469, Sandia National Laboratories, March 1986.

9. J. R. Lee, "Pulse Shaping of High-Current Electron Beams with Gradient B Drift Transport," SAND86-0920, Sandia National Laboratories, May 1986.

10. J. R. Lee, D. L. Faucett, J. A. Halbleib, M. A. Hedemann, and W. A. Stygar, "Reverse-Field Injection for the ∇B Drift Transport of a High-Current Electron Beam," to be published.

11. W. Beezhold, J. Stobbs, W. A. Seidler, R. L. Weitz, D. P. Snowden, and M. A. Hedemann, "Simulation Fidelity Workshop II: Executive Summary," SAND87-1385, Sandia National Laboratories (1987), to be published.

12. C. R. McClenahan, M. A. Hedemann, W. Beezhold, N. E. Counts, T. P. Lynch, D. J. Erven, and J. P. Reilly, "Generating Soft X-Ray Spectra

Using the SPEED Pentaxial Diode," SAND86-0957, Sandia National Laboratories, July 1987.

13. D. C. Iwan, "Computer Simulations of the Ring Diode for Saturn," SAND85-2585, Sandia National Laboratories, May 1986.

14. J. A. Halbleib and T. A. Mehlhorn, Nucl. Sci. Eng., Vol. 92, No. 2, 338 (February 1986). J. A. Halbleib and T. A. Mehlhorn, "ITS: The Integrated TIGER Series of Coupled Electron/Photon Monte Carlo Transport Codes," SAND84-0573, Sandia National Laboratories, November 1984. Also CCC-467, Radiation Shielding Information Center, Computer Code Collection, Oak Ridge National Laboratory [January 1985].

15. G. J. Lockwood, L. E. Ruggles, Glenn H. Miller, and J. A. Halbleib, "Electron Energy and Charge Albedos--Calorimetric Measurement vs Monte Carlo Theory," SAND80-1968, Sandia National Laboratories, November 1981.

16. J. A. Halbleib, Sr., and W. H. Vandevender, J. Appl. Phys. 48, 2312 (1977).

17. J. A. Halbleib, T. W. L. Sanford, and W. Beezhold, "Experimental Verification of Bremsstrahlung Dosimetry Predictions for 0.75 MeV Electrons," SAND85-1517, Sandia National Laboratories, December 1986.

18. T. W. L. Sanford and J. A. Halbleib, IEEE Trans. Nucl. Sci., Vol. NS-31, No. 6, 1094 (1984).

19. J. A. Halbleib and T. W. L. Sanford, "Predicted Flash X-Ray Environments Using Standard Converter Configurations," SAND83-2572, Sandia National Laboratories, September 1985.

20. J. A. Halbleib, J. E. Morel, T. P. Wright, and E. F. Hartman, "Comparison of Deposition Profiles in Generic Configurations From Bremsstrahlung and X-Ray Threat Spectra (U)," SAND81-2559, RS4231/81/14, Sandia National Laboratories, June 1982 (classified).

21. J. A. Halbleib, "Parametric Study of Pulsed Electron Beam Environments," SC-RR-72 0435, Sandia National Laboratories, September 1972.

22. M. J. Berger and S. M. Seltzer, Phys. Rev. C2, 621 (1970).

23. H. W. Koch and J. W. Motz, Rev. Mod. Phys. 31, 920 (1959).

24. J. A. Halbleib, G. J. Lockwood, and G. H. Miller, IEEE Trans.Nucl. Sci. NS-23, 1881 (1976).

25. The unpublished predictions using the improved bremsstrahlung cross sections were for the Ta wrapped TLD data reported in Ref. 29.

26. H. K. Tseng and R. H. Pratt, Phys. Rev. A1, 528 (1970). R. H. Pratt, H. K. Tseng, C. M. Lee, L. Kissel, C. MacCallum, and M. Riley, "Bremsstrahlung energy spectra from electrons of kinetic energy

1 keV $\leq T_1 \leq$ 2000 keV incident on neutral atoms $2 \leq Z \leq 92$," At. Data Nucl. Data Tables 20, 175 (1977); errata in 26, 477 (1981).

27. A. L. Pregenzer and J. A. Halbleib, IEEE Trans. Nucl. Sci. NS-32, No. 6, 4405 (1985).

28. T. W. L. Sanford, J. A. Halbleib, and W. Beezhold, IEEE Trans. Nucl. Sci. NS-32, No. 6, 4410 (1985).

29. T. W. L. Sanford, J. A. Halbleib, W. Beezhold, and L. J. Lorence, IEEE Trans. Nucl. Sci. NS-33, No. 6, 1261 (1986).

30. Proceedings of the DNA/DOE (Sandia) Bremsstrahlung Simulation Fidelity Workshop, May 24-25, 1983, Albuquerque, New Mexico, SAND83-2456, RS3151/83/048, Sandia National Laboratories, edited by W. Beezhold and A. W. Fellows, June 1984, (see pages 21-40 and page 149) (classified).

31. Indeed, we were able to reduce the variance through a slight variation on the FT scheme described in the appendix. We split off a thin downstream layer of the Kevlar debris shield to a thickness of the order of an electron range of the expected photon generated secondary electrons (25, 50, 75, 125 μm at 0.5, 1.0, 1.5, and 2.0 MeV, respectively) and forced X-ray interactions in this layer.

32. G. J. Lockwood, L. E. Ruggles, Glenn H. Miller, and J. A. Halbleib, "Calorimetric Measurement of Electron Energy Deposition in Extended

Media--Theory vs Experiment," SAND79-0414, Sandia National Laboratories, January 1980.

33. ICRU Report 37, "Stopping Powers for Electrons and Positrons," October 1984.

34. J. H. Hubbell, "Photon Cross Sections, Attenuation Coefficients, and Energy Absorption Coefficients from 10 keV to 100 GeV, Report NSRDS-NBS 29 (Washington, DC: U. S. National Bureau of Standards, August 1969) p. 9.

Appendix

Introduction

Experiments that require high doses and dose rates over large volumes involve placing the detector close to the source of radiation. In order to accurately model such experiments, in general, full Monte Carlo transport of electrons and photons must be carried out in both the converter and detector configurations. However, such calculations are very expensive, and, were not possible in many cases until quite recently. In this appendix, we first discuss an approximate method that is useful in certain situations where the detector is in electron equilibrium. We then describe a procedure involving both code modifications and careful choice of input data that makes transport in the full converter/detector geometry possible in those situations where the approximate method is unacceptable. Much of the following has been excerpted from Ref. 27.

Next-Event-Estimator (NE) Method

Under suitable conditions, equilibrium dose in the radiation field of an X-ray simulator driven by a high-intensity pulsed relativistic electron beam can be approximated by the integral over photon energy of the product of the local X-ray flux and the local mass energy absorption coefficient.

In such cases a common procedure is to obtain the X-ray flux from a separate Monte Carlo calculation of the bremsstrahlung production in the converter configuration and to use the output of this calculation to approximate the flux at the detector. Splitting the production and deposition calculations in this fashion is reasonable when the detector is far enough away from the source that a point source approximation is valid. However, when the detector is close to the source, the details of the coupled energy, angle, and spatial distribution of the X rays are important, so that splitting the calculations is no longer acceptable.

We have developed a scheme (NE) that limits the Monte Carlo transport to the converter configuration, including any surrounding support structure, thereby maintaining the efficiency of the decoupled approximation, while using the exact distribution of the X-ray output in the prediction of dose. This is accomplished by including, within the Monte Carlo calculation, a next-event estimator for predicting the dose which is an extension of the next-event estimator that is used in the CYLTRAN code to predict photon escape. This approximation gives the uncollided, equilibrium dose in a detector. Compared with the much more expensive full Monte Carlo transport within the combined converter/detector configuration (discussed below), the NE method has the additional advantage of allowing the dose to be predicted in an arbitrary number of different kinds of detectors at arbitrary locations within a single Monte Carlo run. Consequently, NE has proven to be a very powerful tool for mapping the X-ray dose field for existing X-ray sources and predicting those fields for proposed sources.

In the NE method, the full Monte Carlo transport is only used for the production and transport of X rays throughout the converter configuration, including the electron absorber and debris shield. The detector configuration is not explicitly included in the Monte Carlo transport. Each time a photon emerges from a collision within the converter system traveling in the direction of the detector, its weight is reduced by the probability that it will reach the detector without further collision. We then estimate its contribution to the mean dose in a detector of thickness t,

$$\langle D \rangle = \frac{1}{A\rho t} \int_0^\infty \int_0^{2\pi} h\nu \; \Phi(h\nu, \mathbf{\Omega}) \; \mathbf{\Omega}\cdot\mathbf{n} \; e^{-\tau x/\mathbf{\Omega}\cdot\mathbf{n}} \left[1-e^{-\mu t/\mathbf{\Omega}\cdot\mathbf{n}}\right] \frac{\mu_a(h\nu)}{\mu(h\nu)} \, dh\nu d\mathbf{\Omega}, \quad \text{(A1)}$$

where A is the area of the detector, ρ is the mass density of the detector, $h\nu$ is the photon energy, $\mathbf{\Omega}$ is the photon direction, $\mathbf{n}$ is the unit normal at the detector surface, μ is the attenuation coefficient of the detector, μ_a is the mass energy absorption coefficient of the detector, and x and τ are the thickness and attenuation coefficient, respectively, of any equilibration or filtering material. The quantity $\Phi(h\nu, \mathbf{\Omega})$ is the photon flux at the surface of the detector configuration and is basically the quantity obtained from the Monte Carlo model. The factor $e^{-\tau x/\mathbf{\Omega}\cdot\mathbf{n}}$ accounts for any equilibration or filtering in front of the active region of the detector. The factor $1-e^{-\mu t/\mathbf{\Omega}\cdot\mathbf{n}}$ describes the interaction probability for an active region of thickness t. Taking the limit of Eq. (A1) as $t \to 0$, we obtain

$$D_s = \frac{1}{A\rho} \int_0^\infty \int_0^{2\pi} h\nu \; \Phi(h\nu, \mathbf{\Omega}) \; e^{-\tau x/\mathbf{\Omega}\cdot\mathbf{n}} \; \mu_a(h\nu) \, dh\nu d\mathbf{\Omega}, \quad \text{(A2)}$$

as an estimate for the uncollided surface dose.

The approximation described by Eqs. (A1) and (A2) is a well-known method of estimating energy deposition by low-energy photons. What is novel here, however, is the inclusion of an algorithm for the estimators within the Monte Carlo model itself which insures that the fully coupled, differential (as opposed to histogram approximations) energy, angle, and spatial distribution of the flux is used in evaluating Eqs. (A1) and (A2). The fully coupled model is most important for the sort of close-in exposures expected in Saturn applications. It is less important for far-field ($1/r^2$) exposures where the source is nearly a point source and the radiation incident on the detector is nearly monodirectional. Moreover, the algorithm can easily be written to include the logic for calculating the doses in an arbitrary number of dosimetry configurations within a single Monte Carlo run.

The speed, simplicity, and flexibility of the method make it a powerful tool for predicting X-ray dosimetry under appropriate circumstances. The approximate dose obtained is the uncollided kerma (kinetic energy released in material) dose. The approximation breaks down when;

(a) the detector is so thin that electron equilibrium cannot be established,

(b) photon buildup within the detector configuration itself cannot be neglected,

(c) the photon energy is so high that radiation loss of secondary electrons becomes important, or

(d) an appropriate definition of the mass energy absorption coefficient is not possible.

Difficulty with condition (d) may arise as a consequence of the fact that the mass energy absorption coefficient is not a fundamental physical quantity, but depends on our assumptions about local energy deposition from photon interactions. For electron energies to be encountered at the Saturn facility, we make the conventional assumption that the entire photon energy is absorbed in photoelectric and pair-production interactions, and that the mean energy transferred to the scattered electron is absorbed in an incoherent-scattering interaction. The cross-section generator of the ITS system already contains the logic for generating the mass energy absorption coefficients under these assumptions. Reference 34 provides a more detailed discussion of mass energy absorption coefficients and related quantities.

Full Transport (FT) Method

When any of the above conditions or assumptions are not adequately satisfied, one has no choice but to carry out Monte Carlo transport in the detector itself. However, it is difficult to include within a single Monte Carlo calculation the generation, transport, and subsequent energy deposition from X rays in dosimetry materials without using some fairly sophisticated procedures for variance reduction. The difficulty is caused by the low X-ray conversion efficiency for electrons in this energy range and by the low probability for photon interaction in thin dosimetry configurations.

Some variance reduction procedures are easily accessible via standard code input.[14] For example, one can

(a) scale bremsstrahlung cross sections to increase production efficiency,

(b) terminate the transport of electrons that have little chance of affecting the radiation response of zones outside the one in which they exist (trapped electrons) by simply locally depositing their charge and energy,

(c) reduce excessively high electron populations via Russian Roulette kill, and

(d) force photons to interact in optically thin regions.

These are powerful techniques for certain problems. In the present application, they are used to enhance the number of X rays produced, force those X rays to interact in the detector, and minimize nonessential electron transport. However, except for the forcing of photon interactions, the problem with using the standard options in the present application is that they are global in their effect --- i. e., they operate equally throughout the problem geometry. While it is very efficient to enhance X-ray production in regions of primary electron transport, it is inefficient to do so in the detector where the deposition is dominated by the transport of much lower energy secondary electrons. And while it is efficient to Russian Roulette kill the artificially high population of secondary electrons produced by the enhanced X-ray population in the X-ray source region, it is precisely those electrons that we want to transport in the detector. Conversely, while it is efficient to terminate transport of trapped

electrons in the detector, doing so for the primary electrons would preclude subsequent X-ray production by those electrons.

In order to efficiently carry out FT calculations, we have evolved a set of modifications to the standard options that make their effect contingent upon the spatial location of a given electron. By combining these modifications with careful selection of certain input parameters, we are able to markedly increase the efficiency of the calculations by insuring that those, and only those, variance reduction procedures are operative that are necessary in the converter and detector configurations. The procedure is as follows:

(a) Use the SCALE-BREMS keyword to activate global scaling of bremsstrahlung production and electron impact ionization cross sections; by default this also activates global Russian Rouletting of photon generated secondary electrons back to their natural populations.

(b) Via update, negate biased bremsstrahlung production everywhere except in the region of primary (source) electron transport.

(c) Via update, negate Russian Rouletting of secondary electrons in those regions where they yet may reach the active region of the detector; this normally includes the active portion of the detector, its packaging, and even portions of the converter configuration if electrons photoemitted from those regions can reach the active portion of the detector.

(d) Use the TRAP-ELECTRONS keyword to activate global trapping of all electrons that are found to be more than a range from the nearest

zone boundary by setting the associated energy parameter equal to or greater than the maximum source-electron energy.

(e) Via update, negate trapping of electrons in the region of primary electron transport.

(f) Use the CUTOFFS keyword to set the global electron cutoff to 1.0 keV.

(g) On the data input lines that describe the individual input zones, set the zone dependent electron cutoffs; 5% of the maximum source electron energy in the primary conversion zone (e. g., a tantalum foil), zero in those regions from which electrons may reach the active region of the detector (the code will then internally set them equal to the global electron cutoff), and 10% of the maximum source electron energy in all other problem zones.

(h) On the data input lines that describe the individual input zones from which photon generated secondary electrons may reach the active region of the detector, set the zone dependent photon forcing fractions; e. g., in the upstream-to-downstream sequence Lucite/Al/CaF_2/Al/Lucite simulating the TLD package in Sec. 5.1.1, the corresponding sequence of forcing fractions was 0.05/0.3333/0.5/0.9/0.2.

(i) Via update, increase parameter NLAST which defines the size of the electron bank.

Comparisons of the FT predictions of energy deposition in TLDs with high precision measurements at an electron kinetic energy of 0.75 MeV can be found in Refs. 17 and 28.

Summary

To summarize, photon interactions result in the production of photoelectrons, flourescence photons, Auger electrons, electron-positron pairs, annihilation photons, and Compton scattered photons and electrons. The NE model only transports these secondaries in the converter configuration, whereas the FT model does so for the full converter/detector configuration.

DISTRIBUTION:
Unlimited Release

Aberdeen Proving Ground
BRL, SECAD
Aberdeen, MD 21005
  Attn: A. Prakash

Air Force Cambridge Research Laboratory (3)
L. G. Hanscom Field
Bedford, MA 01730
  Attn: J. C. Garth
        A. R. Frederickson
        J. N. Bradford

Air Force Weapons Laboratory (2)
Kirtland Air Force Base
Albuquerque, NM 87115
  Attn: J. F. Janni, DYC
        J. Mullis

ARCON Corporation
18 Lakeside Office Park
Wakefield, MA 01880
  Attn: S. Woolf

AVCO-Everett Research Laboratory
2385 Revere Beach Parkway
Everett, MA 02149
  Attn: D. Berube

The BDM Corporation
1801 Randolph Rd. SE
Albuquerque, NM 87106
  Attn: C. Wallace

Bhabha Atomic Research Center
Plasma Physics Section
PRIP Shed. Trombay
Bombay-400 085, INDIA
  Attn: T. Vijayan

Boeing Aerospace Co. (3)
P. O. Box 3999
Seattle, WA 98124
  Attn: I. Arimura, M. S. 2R-00
        D. Kelly
        A. Johnston

Anders Brahme
Dept. of Radiation Physics
Karolinska Institute
Fack
S-104 01 Stockholm, SWEDEN

California Institute of Technology
Space Radiation Laboratory
Pasadena, CA 91125
Attn: C. Chen

DARPA
1400 Wilson Blvd.
Arlington, VA 22209
Attn: L. Buchanan

Andree Dutreix
Institut Gustave Roussy
94 800 Villejuif, FRANCE

EMA
1025 Hermosa SE
Albuquerque, NM 87106
Attn: Ezra Mann

Experimental & Mathematical Physics Consultants
Box 3191
Gaithersburg, MD 20878
Attn: T. M. Jordan

J. Z. Farber
Chief, Electronics Vulnerability Division
DNA Headquarters
Attn: RAEV
6801 Telegraph Road
Alexandria, VA 22310

Fulmer Research Institute, Ltd.
STOKE POGES
SLOUGH SL2 4QD
UNITED KINGDOM
Attn: A. Holmes-Siedle

Goddard Space Flight Center
Greenbelt, MD 20771
Attn: N. Gehrels

Grumman Aerospace Corporation (2)
A01-026
Bethpage, NY 11714
Attn: L. Supakoff
M. Stauber

Dietrich Harder
Institut fur Medizinische Physik und Biophysik
D 3400 Gottingen
Gosslerstr. 10, WEST GERMANY

Harry Diamond Laboratories (5)
2800 Powder Mill Road
Aurora Facility
Adelphi, MD 20783
Attn: S. Graybill
K. Karas
D. Whittaker
J. Agee
H. Eisen

Kaman Sciences Corp. (5)
P. O. Box 7463
Colorado Springs, CO 80933
Attn: T. Connolly
D. P. McLemore
R. Zombolla
D. Steele
C. DeJong

Lawrence Livermore National Laboratory (4)
University of California
P. O. Box 808
Livermore, CA 94550
Attn: T. Young
W. Fritchie
G. Vernazza
E. Plechaty

Mr. & Mrs. Hans Leetz
Institut t. Biophysik
Univ. Kliniken
D-6650 Homberg 3, WEST GERMANY

Lockheed Missiles & Space Co.
3251 Hanover St.
Palo Alto, CA 94304
Attn: M. D. Castillo

Los Alamos National Laboratory (6)
P. O. Box 1663
Los Alamos, NM 87544
Attn: J. Mack
J. E. Morel
M. Jain
H. G. Hughes
H. H. Hsu
R. Schrandt

LTV Missiles and Electronics Group
P. O. Box 650003
Dallas, TX 75265-0003
Attn: R. Melin

M. D. Anderson Hospital
Physics Department
Texas Medical Center
Houston, TX 77030
Attn: Peter Almond

McDonnell Douglas (2)
Astronautics Company-East
St. Louis, MO 63166
Attn: G. W. Davis
R. L. Kloster

McDonnell Douglas Astronautics Co.
5301 Bolsa Avenue
Huntington Beach, CA 92647
Attn: M. R. Westmorland

Mission Research Corporation (2)
5434 Ruffin Road
San Diego, CA 92123
Attn: V. A. J. Van Lint
D. Snowden

Mission Research Corporation
735 State Street
Santa Barbara, CA 93101
Attn: C. L. Longmire

Mission Research Corporation (2)
1720 Randolph Ave. NE
Albuquerque, NM 87106
Attn: B. Godfrey
J. Clifford

NASA Langley Research Center
Hampton, VA 23665
Attn: C. K. Chang, 160

National Research Council of Canada (2)
Division of Physics
Ionizing Radiation Standards Section
Ottawa, Ontario KIA OR6
CANADA
Attn: D. W. O. Rogers
A. Bielajew

Naval Surface Weapons Center (4)
Code R-41
Silver Springs, MD 20910
Attn: M. Eha
O. Goktepe
D. Rule
V. Kenyon

Naval Weapons Support Center
Code 6054
Crane, IN 47522
Attn: J. L. Ramsey

Orlando Technologies, Inc. (2)
1651 University, NE
Albuquerque, NM 87102
Attn: J. Prentiss
D. Matuska

Physics International (4)
2700 Merced Street
San Leandro, CA 94577
Attn: J. E. Faulkner
D. L. Shaeffer
C. Gilman
J. Creedon

Princeton Plasma Physics Laboratory
P. O. Box 451
Princeton, NJ 08544
Attn: Seng Liek Liew, Bldg. 1-P

Science Applications International Corp.
2109 Air Park Road SE
Albuquerque, NM 87106
Attn: R. L. Weitz

Science Applications International Corp.
P. O. Box 2351
1250 Prospect Street
La Jolla, CA 92037
Attn: W. H. Scott, Jr.

Science Applications International Corp. (5)
P. O. Box 1303
1710 Goodridge Dr.
McLean, VA 22102
Attn: W. L. Chadsey
K. Adams
J. E. Tigner
A. A. Mondelli
D. Bacon

Science Applications International Corp.
10210 Campus Point Drive
San Diego, CA 92121
Attn: D. G. Millward
J. R. Florian

SPIRE Corporation
Patriots Park
Bedford, MA 01730
Attn: R. Little

Stanford Linear Accelerator Center
Radiation Physics Group, Bin48
P. O. Box 4349
Stanford, CA 94306
Attn: W. R. Nelson

Texas A&M University
2703 Jennifer Circle
College Station, TX 77840
Attn: R. R. Hart

Thomas Jefferson University Hospital
Dept. Rad. Therapy and Nuclear Med.
10th & Walnut Streets
Philadelphia, PA 19107
Attn: K. Ayyangar

Titan Systems Inc.
Suite 370
39510 Paseo Padre Pkwy.
Fremont, CA 94538
Attn: K. Billman

TRW (2)
1 Space Park
134/9048
Redondo Beach, CA 90278
Attn: M. Bronstein
G. McKinney

U.S. Naval Research Laboratory (3)
Code 6651
Washington, DC 20375
Attn: G. Herling
D. Brown
C. M. Dozier

U.S. Department of Commerce (6)
National Bureau of Standards
Washington, DC 20234
Attn: M. J Berger
S. M. Seltzer
G. Barnea, 533
R. S. Caswell
S. E. Chappell
J. W. Motz

University of Umea (2)
Radiation Physics Dept.
S-901 85 UMEA
SWEDEN
Attn: A. Nahum
H. Svensson

Andre Wambersie
Unite de Radiotherapie et de Neutrontherapie
Centre des Tumerus UCL 54.69
av. Hippocrate, 54
B. 1200 Bruxelles, BELGIUM

White Sands Missile Range (3)
Nuclear Effects Lab
P. O. Box 477
White Sands, NM 88002
Attn: J. L. Meason
T. M. Flanders
W. W. Sallee

Dr. G. Yonas, President
Titan Corporation
9191 Townecenter Drive
San Diego, CA 92122

The Ontario Cancer Institute
500 Sherbourne St.
Toronto
CANADA M4X 1K9
Attn: M. K. Woo

Science Research Corp.
1010 Memorial Drive
Cambridge, MA 02138
Attn: J. H. Jacob

Pulse Sciences, Inc. (8)
600 McCormick St.
San Leandro, CA 94577
Attn: R. G. Altes
V. Bailey
P. Corcoran
D. L. Pellon
S. Putnam
L. G. Schlitt
I. Smith
P. W. Spence

Berkeley Research Associates
P.O. Box 852
Springfield, VA 22150
Attn: N. R. Pereira

S-CUBED
3398 Carmel Mountain Rd.
San Diego, CA 92121
Attn: M. Merker

IRT Corporation
3030 Callan Road
San Diego, CA 92121
Attn: D. Frederick

AWRE (3)
Aldermaston
Reading RG7 4PR
Berkshire, ENGLAND
Attn: A. C. Douglas
E. M. Gunnersen
C. Martin

Maxwell Laboratories, Inc. (3)
9244 Balboa Ave.
San Diego, CA 92123
Attn: J. E. Rauch
M. Montgomery
K. Ware

JAYCOR (2)
P. O. Box 85154
San Diego, CA 92138
Attn: W. Seidler
B. C. Passenheim

E. A. Burke
Mission Research Corp.
74 Northeastern Blvd.
Nashua, NH 03062

Mr. J. Harrity
IRT Corp.
P. O. Box 80817
San Diego, CA 92138

Mr. K. C. Humphreys
Vice President
Far West Technology, Inc.
330 D. So. Kellogg
Goleta, CA 93117

Dr. K. Mehta
Atomic Energy of Canada Ltd.
Pinawa, Manitoba
CANADA, ROE 1L

G. Messenger
3111 Bel Air Drive
Las Vegas, NV 89109

L. J. Palkuti
ARACOR
1223 E. Arques Ave.
Sunnyvale, CA 94086

Dr. Eligius Wolicki
Kaman Tempo
2560 Huntington Ave.
Suite 500
Alexandria, VA 22303

1200 J. P. VanDevender
1230 J. E. Powell
1231 J. R. Lee (10)
1231 J. A. Halbleib (20)
1231 V. J. Harper-Slaboszewicz
1231 R. P. Kensek
1231 L. J. Lorence
1231 A. L. Pregenzer
1231 T. W. L. Sanford
1232 W. Beezhold
1232 W. P. Ballard
1232 D. E. Beutler
1233 L. M. Choate
1233 G. A. Carlson
1233 M. A. Hedemann
1233 C. R. McClenahan
1233 J. Reilly
1233-1 W. McAtee
1233-1 F. Reynolds
1233-1 A. W. Sharpe
1233-1 T. Thornhill
1233-1 B. Henderson, Ktech

1233-1 A. Schmidlapp, Ktech
1234 R. J. Leeper
Attn: Staff
1234 G. T. Baldwin
1234 L. P. Mix
1235 J. M. Hoffman
1236 G. A. Zawadzkas
1240 K. R. Prestwich
1241 J. R. Freeman
Attn: Staff
1245 J. J. Ramirez
Attn: Staff
1250 T. H. Martin
1251 E. L. Burgess
1251 J. D. Boyes
1251 J. J. Robischon
1252 B. N. Turman
1252 D. D. Bloomquist
1253 D. H. McDaniel
1260 D. L. Cook
1261 M. J. Clauser
1261 C. J. MacCallum
1263 J. N. Olsen
1264 R. W. Stinnett
1265 J. P. Quintenz
Attn: Staff
1265 T. A. Mehlhorn
1265 M. A. Sweeney
1270 J. K. Rice
1272 D. E. Hasti
Attn: Staff
1273 M. K. Matzen
Attn: Staff
1274 R. J. Lipinski
1512 D. A. Benson
1522 E. D. Reedy, Jr.
2100 B. L. Gregory
2120 E. G. Franzak
2126 J. E. Gover
Attn: Staff
2140 C. F. Gibbon
Attn: staff
2300 J. L. Wirth
2310 M. K. Parsons
Attn: Staff
2320 J. H. Renken
2321 E. F Hartman
Attn: Staff
2321 C. Drumm
2321 T. A. Haill
2321 J. J. Hohlfelder
2321 L. D. Posey
2322 G. J. Scrivner
Attn: Staff

2322 W. C. Fan
2322 S. B. Roeske
2322 C. N. Vittitoe
2330 J. H. Stichman
Attn: Staff
2340 M. W. Callahan
Attn: Staff
2360 P. A. Longmire
Attn: Staff
3141 S. A. Landenberger (5)
3151 W. L. Garner (3)
3154-1 DOE/TIC (28)
3312 T. N. Simmons
5100 J. C. Crawford
Attn: Staff
5150 K. D. Hardin
Attn: Staff
5152 J. L. Duncan
6447 W. H. Buckalew
6452 D. W. Vehar
6454 J. G. Kelly
6512 F. J. Wyant
7110 J. D. Plimpton
7111 J. R. Banister
7112 C. R. Mehl
Attn: Staff
7112 T. J. Tanaka
7112 J. Harris
7866 K. W. Hanks
8024 P. W. Dean
8130 E. E. Ives
8340 W. Baur
8341 A. J. Antolak
9112 S. A. Dupree
Attn: Staff
9112 H. M. Sanger